Using ALMA to resolve the nature of the early star-forming large-scale structure PLCK G073.4–57.5

Rüdiger Kneissl, Maria del Carmen Polletta, Clement Martinache, Ryley Hill, Benjamin Clarenc, Herve Dole, Nicole P. H. Nesvadba, Douglas Scott, Matthieu Bethermin, Brenda Frye, et al.

Astronomy & Astrophysics manuscript no. ALMA˙G073˙v6
April 19, 2018

Using ALMA to resolve the nature of the early star-forming large-scale structure PLCK G073.4−57.5

Rüdiger Kneissl[1,2], Maria del Carmen Polletta[3,4], Clement Martinache[5,6], Ryley Hill[7], Benjamin Clarenc[5], Herve A. Dole[5], Nicole P.H. Nesvadba[5], Douglas Scott[7], Matthieu Béthermin[8,9], Brenda Frye[10], Martin Giard[4], Guilaine Lagache[9], and Ludovic Montier[4]

[1] European Southern Observatory, ESO Vitacura, Alonso de Cordova 3107, Vitacura, Casilla, 19001, Santiago, Chile
[2] Atacama Large Millimetre/submillimetre Array, ALMA Santiago Central Offices, Alonso de Cordova 3107, Vitacura, Casilla, 763 0355, Santiago, Chile e-mail: ruediger.kneissl@alma.cl
[3] INAF – Istituto di Astrofisica Spaziale e Fisica Cosmica Milano, via E. Bassini 15, 20133 Milano, Italy
[4] IRAP, Université de Toulouse, CNRS, CNES, UPS, (Toulouse), France
[5] Institut d'Astrophysique Spatiale, CNRS (UMR 8617) Université Paris-Sud 11, Bâtiment 121, 91405, Orsay, France
[6] Departamento de Astronomía, Universidad de Concepción, Avenida Esteban Iturra s/n, Casilla 160-C, Concepción, Chile
[7] Department of Physics and Astronomy, University of British Columbia, 6224 Agricultural Road, Vancouver BC V6T 1Z1, Canada
[8] European Southern Observatory, Karl-Schwarzschild-Straße 2, D-85748 Garching, Germany
[9] Aix Marseille Univ, CNRS, LAM, Laboratoire d'Astrophysique de Marseille, Marseille, France
[10] Steward Observatory, University of Arizona, Tucson, AZ, 85721, USA

Received / Accepted

ABSTRACT

Galaxy clusters at high redshifts are key targets for understanding matter assembly in the early Universe, yet they are challenging to locate. A sample of more than 2000 high-z candidate structures have been found using *Planck*'s all-sky submillimetre maps, and a subset of 234 have been followed up with *Herschel*-SPIRE, which showed that the emission can be attributed to large overdensities of dusty star-forming galaxies. However, the individual galaxies giving rise to the emission seen by *Planck* and *Herschel* have not yet been resolved nor characterized, so we do not know whether they constitute the progenitors of present-day, massive galaxy clusters. In an attempt to address this, we targeted the eight brightest *Herschel*-SPIRE sources in the centre of the *Planck* peak G073.4−57.5 using ALMA at 1.3 mm, and complemented these observations with multi-wavelength data from *Spitzer*-IRAC, CFHT-WIRCam J, K, and JCMT's SCUBA-2 instrument. We detect a total of 18 millimetre galaxies brighter than 0.3 mJy in 2.4 arcmin^2. The ALMA source density is 8–30 times higher than average background estimates, and larger than seen in typical "proto-cluster" fields. We are able to match all but one ALMA sources to their NIR counterparts. The most significant (four) SCUBA-2 sources are not included in the ALMA pointings, but we find an $8\,\sigma$ stacking detection of the ALMA sources in the SCUBA-2 map at 850 μm. We derive photometric redshifts, IR luminosities, star-formation rates, stellar masses, dust temperatures, and dust masses for all the ALMA galaxies; the photometric redshifts are concentrated around $z \simeq 1.5$ and the near-IR colours show a "red" sequence, while the star-formation rates indicate that one third of the galaxies are "starbursts," the others being main-sequence star-forming galaxies. Serendipitous CO line detections of two of the galaxies appear to match their photometric redshifts, with $z = 1.54$. We thus find that the *Planck* peak G073.4−57.5 contains a proto-cluster candidate at $z = 1.54$, and one of the richest regions of ALMA sources known. The ALMA-detected members are massive galaxies on the main-sequence relation and account for a total star-formation rate of at least 1000 $M_\odot$ yr^{-1}.

Key words. Large-scale structure of Universe – Submillimetre: galaxies – Radio continuum: galaxies – Radio lines: galaxies – Galaxies: star formation

1. Introduction

Hierarchical clustering models of large-scale structure and galaxy formation predict that the progenitors of the most massive galaxies in today's clusters are dusty star-forming galaxies at high redshift ($z \simeq$ 2-3, e.g., Lilly et al. 1999; Swinbank et al. 2008). Observationally, this picture is supported by the clustering measurements (Blain et al. 2004) of submillimetre galaxies (SMGs), and by their relative abundance and distribution in known proto-clusters (e.g., Capak et al. 2011; Hayashi et al. 2012; Casey et al. 2015; Hatch et al. 2016; Overzier 2016), while recent studies may also indicate a complicated evolution (e.g., Hayashi et al. 2017). High-redshift structure formation studies in millimetre (mm) and submillimetre (submm) wavelength ranges have the advantage of providing access to high redshifts by utilizing the steep rise in the warm dust spectrum of infrared galaxies (the "negative k-correction," Blain & Longair 1993; see also Guiderdoni et al. 1997) and can build on an observed correlation between the total matter density and the cosmic infrared background fluctuations (Planck Collaboration et al. 2014b).

Substantial progress has been made on probing the early formation of massive structures and galaxy clusters through mm/submm observations (see Casey 2016, for a recent discussion), with a strong emphasis on main-sequence evolution versus starbursts and mergers (see also Narayanan et al. 2015). Mechanisms for rapid, episodic bursts, suggested to explain how the member galaxies are assembled and grow during cluster formation, can be tested with measurements of mm galaxy number densities and gas depletion timescales in cluster-forming environments. Likewise, the processes responsible for triggering star

formation that is coherent over large spatial scales may depend on environmental effects, which can only be tested using a variety of high quality data over wide areas.

The *Planck* satellite mapped out the whole sky between 30 and 857 GHz with a beam going down to 5′ (Planck Collaboration et al. 2014a), giving it the capability of detecting the brightest mm/submm regions of the extragalactic sky at Mpc scales. A component-separation procedure using a combination of *Planck* and IRAS data was applied to the maps outside of the Galactic mask to select over 2000 of the most luminous submm peaks in the cosmic infrared background (CIB), with spectral energy distributions peaking between 353 and 857 GHz (Planck Collaboration et al. 2016b, the "PHz" catalogue). 234 of these peaks (chosen such that S/N > 4 at 545 GHz, $S_{857}/S_{545} < 1.5$, and $S_{217} < S_{353}$) were subsequently followed up with *Herschel*-SPIRE observations between 250 and 500 μm, and the half-arcminute (or better) resolution was capable of distinguishing between bright gravitational lenses and concentrations of clustered mm/submm galaxies around redshifts of 2–3 (Planck Collaboration et al. 2015). Here, we present the first detailed mm analysis of one of these highly clustered regions, PLCK G073.4−57.5 (hereafter G073.4−57.5), which was observed with ALMA in Cycle 2. We combine NIR and FIR multi-wavelength data with the resolving power of ALMA to identify the individual galaxies responsible for much of the *Planck* submm flux and to constrain their physical properties.

This paper on G073.4−57.5 is structured as follows. In Sect. 2 we re-capitulate the features of the *Planck*/*Herschel* sample, followed by Sect. 3, where we present details of the ALMA observations, data reduction, and results. In Sect. 4 we describe the set of multi-wavelength data on G073.4−57.5, comprising *Herschel*-SPIRE, SCUBA-2, *Spitzer*-IRAC, and CFHT-WIRCam observations. In Sect. 5 we present the analysis of these data, where we estimate the mm galaxy number density of G073.4−57.5, derive photometric redshifts and IR properties of each galaxy (such as dust temperature, dust mass, IR luminosity, star-formation rate and stellar mass), and in Sect. 6 we interpret serendipitous line detections. In Sect. 7 we discuss our findings and synthesize the interpretation. The paper is then concluded in Sect. 8.

Throughout this paper we use the parameters of the best-fit *Planck* flat ΛCDM cosmology (Planck Collaboration et al. 2016a), i.e., $\Omega_M = 0.308, h = 0.678$, and note that in this model 1″ at $z = 1.5$ corresponds to a physical scale of 8.7 kpc.

2. The *Planck*/*Herschel* high-z sample

A dedicated *Herschel* (Pilbratt et al. 2010) follow-up programme with the SPIRE instrument for 234 *Planck* targets (Planck Collaboration et al. 2015) found a significant excess of "red" sources (where "red" means $S_{350}/S_{250} > 0.7$ and $S_{500}/S_{350} > 0.6$ (consistent with $z \geq 2$), in comparison to reference SPIRE fields. Assuming a single common dust temperature for the sources of $T_d = 35$ K, IR luminosities of typically 4×10^{12} $L_\odot$ were derived for each SPIRE source, yielding star-formation rates (SFRs) of around 700 $M_\odot$ yr^{-1}. If these observed *Herschel* overdensities are coherent structures, their total IR luminosity would peak at 4×10^{13} $L_\odot$, or in terms of SFR, at 7×10^3 $M_\odot$ yr^{-1}, i.e., the equivalent of ten typical sources constituting to the overdensity.

A small subset of 11 *Herschel* sources are now known to be gravitationally lensed single galaxies (Cañameras et al. 2015), including the extremely bright G244.8+54.9, greater than 1 Jy at 350 μm. ALMA data for such sources, also aided by *HST*-based lensing models, have enabled extremely detailed studies of high-z star-forming galaxies (e.g., Nesvadba et al. 2016; Cañameras et al. 2017a,b).

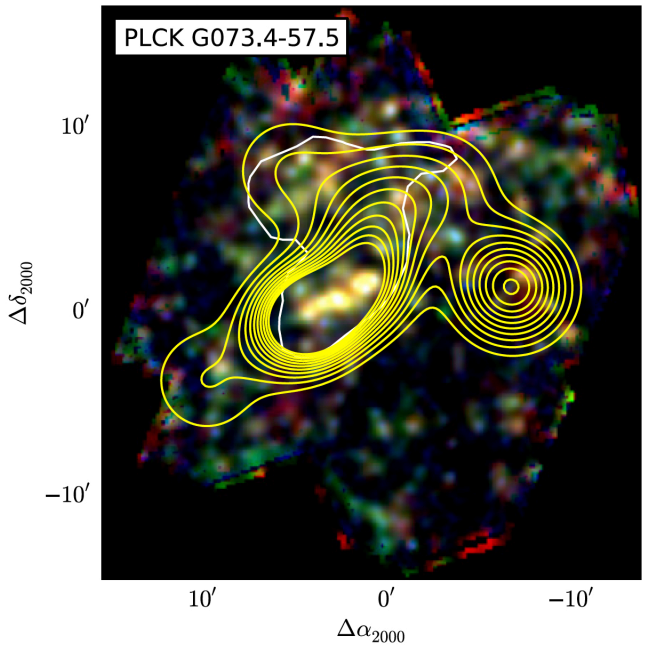

Fig. 1. 3-colour SPIRE image for G073.4−57.5 (taken from Planck Collaboration et al. 2015): blue, 250 μm; green, 350 μm; and red, 500 μm. The white contour shows the region encompassing 50 % of the *Planck* flux density, while the yellow contours are the significance of the overdensity of red (350 μm) sources, plotted starting at 2 σ with 1 σ incremental steps.

In a recent paper, MacKenzie et al. (2017) presented SCUBA-2 follow-up of 61 *Planck*/*Herschel* targets at 850 μm, each observation covering essentially the full emission of the *Planck* peak. 172 sources were detected in the maps with high confidence (S/N > 4.5), and by fitting modified blackbody dust SEDs it was shown that the distribution of photometric redshifts peaks between $z = 2$ and $z = 3$.

Further studies of the *Planck*/*Herschel* targets, based on NIR and optical data, have also been carried out (e.g., G95.5−61.6 by Flores-Cacho et al. 2016) or are in progress (e.g., a sample by Martinache 2016) with the aim of characterizing these sources; indeed, Flores-Cacho et al. (2016) was able to conclude that G95.5−61.6 consists of two significantly clustered regions at $z \simeq 1.7$ and at $z \simeq 2.0$, which further motivates their utility for studying high-redshift clustering.

In the current paper we focus on directly detecting the galaxies responsible for giving rise to the *Planck* peak using the high-resolution (sub-)mm imaging capabilities of ALMA. Our target G073.4−57.5 was included in the *Planck*/*Herschel* sample from the selection of the first public release data of the *Planck* Catalogue of Compact Sources[1] with a 545-GHz (PSF FLUX) flux density of (731 ± 81) mJy. It was chosen for an ALMA proposal, together with three other *Planck*/*Herschel* targets, based on the high overdensity of *Herschel* sources within the *Planck* contour (see Fig. 1) and the availability of additional NIR and submm data.

[1]Note, that for the latest *Planck* release(Planck Collaboration et al. 2016b), G073.4−57.5 lies just inside the more conservatively applied Galactic mask.

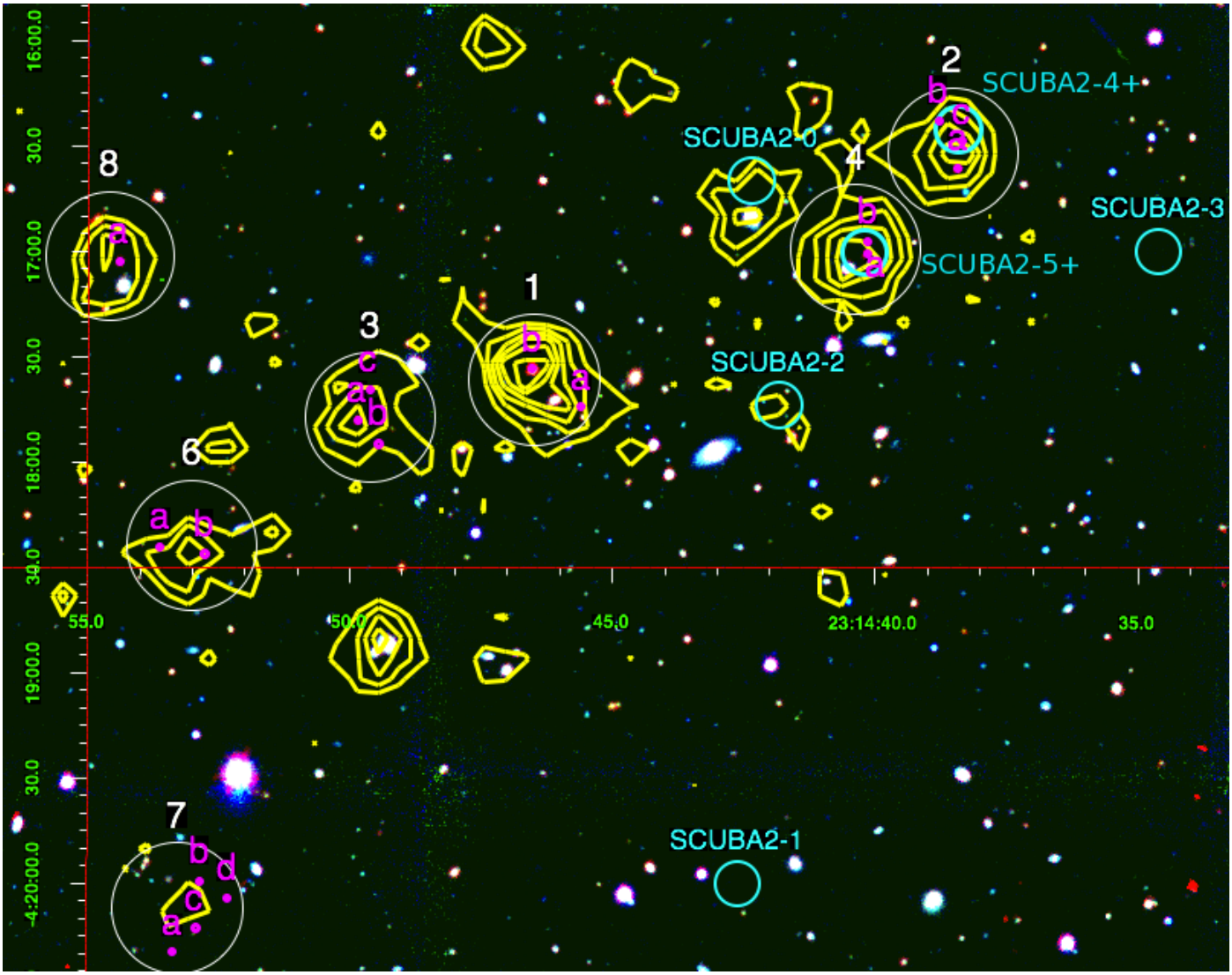

Fig. 2. Central region ($5.8' \times 4.6'$) of G073.4−57.5 in a 3-colour image of *Spitzer*-IRAC 3.6 μm (red), VLT-HAWKI K-band (green) and J-band (blue), with *Herschel*-SPIRE 250-μm thick contours in yellow (from 0.02 Jy beam^{-1} in 0.0125 Jy beam^{-1} steps) and ALMA galaxy positions shown with magenta circles of radius 0.7″. The ALMA areas that were used for the analysis (0.2 × primary beam peak response) are indicated with thin white circles (37″ diameter), labelled according to their field IDs given in Table 2. Four SCUBA-2 sources centred in the cyan circles (13″ diameter matching the beam size) are labelled according to MacKenzie et al. (2017); the two SCUBA-2 sources labeled "4+ / 5+" are additionally selected as $> 3\,\sigma$ peaks in the SCUBA-2 maps coincident with ALMA-detected sources. ALMA field 5 (with one detected source, see Fig. 3) is located above and to the right of the central region and is not shown in this image.

3. ALMA observation of G073.4−57.5

We received 0.4 hours of on-source observing time on G073.4−57.5 with ALMA in Cycle 2 (PID: 2013.1.01173.S, PI R. Kneissl). We targeted the eight sources found in the SPIRE field that were consistent with a "red" colour, within the error bar, as defined above. A standard Band 6 continuum set-up around 233 GHz (1.3 mm) was used, with four 1.78-GHz spectral windows divided into the two receiver sidebands, separated by 16 GHz (i.e., central frequencies of 224, 226, 240 and 242 GHz). 34 antennas were available in the array configuration during the time of the observation, and the resulting synthesized beam achieved an angular resolution of 0.56″ × 0.44″ (FWHM) with a position angle of −82.7°. The central sensitivity was $\simeq 0.06$ mJy beam^{-1} in all eight fields (see Fig. 2 for an overview, and note the *Herschel* SPIRE IDs, as given in Table 2); with this sensitivity ALMA can detect all SPIRE sources at any redshift assuming a dust temperature of > 25 K and that all the SPIRE flux comes from a single source, since the detection significance increases at higher redshifts and with higher temperatures. The observatory standard calibration was used with J2232+1143, a grid monitoring source, as bandpass calibrator, Ceres as additional flux calibrator, and all pointings in this data set share the same phase calibrator, J2306−0459. The single pointings were convolved with the primary antenna beam pattern (roughly Gaussian with FWHM $\simeq 25.3''$, assuming $1.13\lambda/D$).

The data were reduced with standard `CASA` tasks (McMullin et al. 2007), including de-convolution, to yield calibrated continuum images with flat noise characteristics for source detection. A S/N > 5 mask was applied to the beam-uncorrected maps with a $2\,\sigma$ `CLEAN` threshold, yielding 13 sources in six fields, where the detection is based on the peak pixel surface bright-

ness. In addition, the single brightest sources from each of the remaining two fields were included in the sample, since they were both well centred, with S/N > 4.5. During cross-matching with *Spitzer* maps, three additional sources were identified with S/N > 4.5. The final sample, containing 18 ALMA sources with flux densities > 0.3 mJy and S/N > 4.5, is presented in Table 1.

The flux density results were derived from applying `ImageFitter` to the `CLEAN`ed maps and integrating over each source. They are presented in Table 1, along with the angular sizes for nine sources that were best fit with an extended profile (and four of which had a major axis determined with S/N > 3). In the nine remaining cases the fit for size did not converge well and these are listed as point sources. In addition, for each source we give the peak flux density at 233 GHz from the beam de-convolved map (which is more accurate for the nine point sources) and the coordinate for the position of the peak surface brightness. Note that ALMA source ID 16, which is on the edge of pointing field 7, has a recovered peak flux density of (0.59 ± 0.17) mJy beam^{-1}, i.e., 3.5 σ, and should thus be considered tentative, in spite of the match with a *Spitzer* source (see next section, Fig. 3).

4. Multi-waveband data

4.1. Dust Spectral Energy Distributions

For the analysis of the spectral energy distributions (SEDs) of the far-infrared part of our multi-waveband data we used a modified blackbody spectrum given by $L_\nu = N\,4\pi a^2\,Q_\nu(a)\,\pi B_\nu(T)$, where $Q_\nu(a) = (2\pi a\nu/c)^\beta$, $B_\nu(T)$ is the Planck spectrum, N the number of grains, and a the grain size half-diameter.[2] Note, that a submm dust opacity spectral index of $\beta \simeq 2.0$ is widely used, and lies within the range of theoretical models (Draine 2011) as well as empirical fits to nearby galaxies (e.g., Clements et al. 2010), and is close to the local ISM value (Planck Collaboration et al. 2011). In terms of observed flux density[3] this gives

$$S_\nu = N a^{2+\beta}\,\frac{(2\pi)^{1+\beta}\,h}{c^{2+\beta}}\,\frac{\nu^{3+\beta}\,(1+z)^{4+\beta}\,D_{\rm L}^{-2}}{\exp[h\nu\,(1+z)\,/\,(kT_{\rm d})]-1}, \qquad (1)$$

where $D_{\rm L}$ is the luminosity distance. Following Scoville et al. (2014, 2016) we can use a direct, normalized dependence on the interstellar medium (ISM, i.e., H I and H_2 + He) mass, with $\kappa_\nu({\rm ISM})/\kappa_\nu({\rm dust}) = M_{\rm ISM}/M_{\rm dust}$ ($\simeq 100$). Then

$$S_\nu = \frac{1.17\,x}{e^x-1}\,\frac{M_{\rm ISM}}{10^{10}{\rm M}_\odot}\left(\frac{\nu}{353\,{\rm GHz}}\right)^{2+\beta}(1+z)^{3+\beta}\left(\frac{\rm Gpc}{D_{\rm L}}\right)^2\,{\rm mJy}, \qquad (2)$$

where $x = 0.484\,(35\,{\rm K}/T_{\rm d})\,(\nu/353\,{\rm GHz})\,(1+z)$.

4.2. Herschel-SPIRE

G073.4−57.5 was observed with *Herschel*-SPIRE at 250, 350, and 500 μm (where the corresponding spatial resolutions are 18, 25, and 36 arcsec, respectively) as part of the dedicated follow-up program of 234 *Planck* sources (Planck Collaboration et al. 2015). The images reached 1 σ (instrument + confusion) noise levels of 9.9 mJy at 250 μm, 9.3 mJy at 350 μm, and 10.7 mJy at 500 μm.

As discussed in the previous section, the SPIRE analysis revealed the presence of several "red" sources, compatible with a $z \approx 2$ structure, centred at SPIRE source ID 7 (i.e., ALMA field 3) and highly elongated in the NW-SE direction. A modified blackbody fit only with the *Herschel* data to SPIRE sources 3, 7, and 15 (ALMA fields 2, 3, and 6) was consistent with $z \simeq 2$, assuming a dust temperature of $T_{\rm d} = 35$ K. Table 2 lists the SPIRE sources targeted with ALMA, along with their measured flux densities at 350 μm, the colours relative to 250 and 500 μm, and the sum per field of the 1.3-mm flux density resolved into the individual galaxies seen with ALMA.

4.3. JCMT SCUBA-2

As part of a SCUBA-2 follow-up of 61 *Planck* high-z candidates (MacKenzie et al. 2017), G073.4−57.5 was observed at 850 μm with approximately 10′ diameter "daisy"-pattern scans, thus covering the whole *Planck* region. The match-filtered image reached a minimum rms depth of 1.6 mJy beam^{-1}. Table 3 lists the sources identified in MacKenzie et al. (2017), as well as their peak flux densities. These include all sources with S/N > 4 and $S_{850} > 7$ mJy. We also include two additional sources we have identified as having pronounced flux density peaks coincident the detected ALMA sources in fields 2 and 4, but with 3 < S/N < 4 in the SCUBA-2 data. These two additional, lower significance SCUBA-2 sources (labelled "4+" and "5+" in Table 3 and Fig. 2) are well matched to ALMA sources (although blended in the SCUBA-2 map). The apparent clustering of SCUBA-2 sources in Fig. 2 may indicate a physical concentration of bright submm source around ALMA field 4. The ratios of the integrated flux densities, ALMA / SCUBA-2, for ALMA fields 2 and 4 are consistent with the modified blackbody spectrum for $z = 2.0$, $\beta = 2.0$ and $T = 30$ K. Conversely, for the other ALMA sources we would not necessarily expect strong individual detections in the SCUBA-2 data, given the sensitivity and confusion levels. Because of this we performed a stacking analysis by summing the flux densities in the beam-convolved SCUBA-2 map at the positions of all the ALMA-detected mm sources, obtaining a significant signal of (56 ± 11) mJy, or (4.0 ± 0.5) mJy per source from a weighted average.

4.4. Spitzer IRAC

G073.4−57.5 was observed with *Spitzer*-IRAC in GO11 (PID: 80238, by PI H. Dole), along with 19 other promising (i.e., high S/N and "red") *Planck* sources with complimentary *Herschel* data. The observations involved a net integration time of 1200 s per (central) sky pixel at 3.6 μm (hereafter "channel 1") and 4.5 μm (hereafter "channel 2") over an area of about 5′ × 5′, and two additional side fields of the same area covered only in channel 1 or in channel 2. The area mapped in both channels is well matched to the angular size of one *Planck* beam and covers the full area of interest.

Source extraction in the IRAC mosaics was performed using `SExtractor` (Bertin & Arnouts 1996), with the IRAC-optimized parameters of Lacy et al. (2005). The detection threshold was set to 2 σ. A choice was made not to filter the image due to the high density of sources. Photometry was performed using the `SExtractor` dual mode with the channel 2 mosaic as the detection image. Given the relative depth of channel 1 compared to channel 2, a detection at the longer wavelength can be sufficient to confirm that the source is red (i.e., selecting galaxies at $z > 1.3$, cf. Papovich 2008), where "red" in this context is

[2] While we show here that a physically motivated approach exists, we stress that we use the resulting equation in a phenomenological sense, i.e., with a single normalization factor per source.

[3] $S_\nu = (1+z)\,(L_{(1+z)\nu}/L_\nu)\,L_\nu/(4\pi D_{\rm L}^2)$.

Table 1. Basic properties of the ALMA galaxies detected at 1.3 mm in G073.4−57.5.

ID (field)	Name / Position[a] [ICRS]	S_ν (peak)[b] [mJy beam^{-1}]	S/N[c]	S_ν (integr.)[d] [mJy]	Size[e] [arcsec]
0 (1b)	ALMAU J231446.53−041733.5	0.58 ± 0.07	7.4	**1.2** ± 0.2	0.65/(0.40)
1 (1a)	ALMAU J231445.60−041744.4	1.45 ± 0.20	7.5	**2.4** ± 0.5	(0.50/0.30)
2 (2b)	ALMAU J231438.78−041622.7	0.90 ± 0.09	10.3	**1.6** ± 0.2	0.61/(0.20)
3 (2a)	ALMAU J231438.42−041636.2	1.08 ± 0.06	14.8	**1.7** ± 0.1	0.44/(0.26)
4 (2c)	ALMAU J231438.36−041628.4	**0.42** ± 0.06	5.6	0.5 ± 0.1	p
5 (3a)	ALMAU J231449.85−041748.1	1.17 ± 0.07	22.5	**1.4** ± 0.1	(0.28/0.20)
6 (3c)	ALMAU J231449.63−041739.3	**0.33** ± 0.06	4.9	0.4 ± 0.1	p
7 (3b)	ALMAU J231449.45−041754.7	**0.34** ± 0.06	5.0	0.3 ± 0.1	p
8 (4a)	ALMAU J231440.15−041700.7	0.93 ± 0.06	14.7	**1.3** ± 0.1	0.47/(0.15)
9 (4b)	ALMAU J231440.14−041657.2	0.25 ± 0.06	5.0	**0.6** ± 0.2	(0.97/0.27)
10 (5a)	ALMAU J231437.03−041451.7	0.35 ± 0.07	4.6	**0.6** ± 0.2	(0.53/0.22)
11 (6a)	ALMAU J231453.61−041823.9	**0.93** ± 0.09	6.9	1.1 ± 0.2	p
12 (6b)	ALMAU J231452.78−041826.1	**0.67** ± 0.06	6.1	0.9 ± 0.1	p
13 (7a)	ALMAU J231453.37−042019.5	0.99 ± 0.12	6.0	**1.7** ± 0.3	(0.49/0.38)
14 (7b)	ALMAU J231452.86−041959.3	**0.75** ± 0.09	5.5	0.7 ± 0.1	p
15 (7c)	ALMAU J231452.94−042012.7	**0.59** ± 0.10	4.9	0.7 ± 0.2	p
16 (7d)	ALMAU J231452.34−042004.2	**0.59** ± 0.17	4.8	0.7 ± 0.4	p
17 (8a)	ALMAU J231454.38−041702.9	**0.53** ± 0.07	4.6	0.7 ± 0.1	p

[a] Coordinate errors on the ALMA positions are approximately 0.5″/ S/N, i.e., 0.1″ or better.
[b] Peak flux density (primary beam de-convolved). The values in bold font are for unresolved sources, and can be considered more reliable.
[c] S/N ratio in the primary beam-convolved, CLEANed detection maps.
[d] Integrated flux density (primary beam de-convolved, image fit). The values in bold font are for resolved sources, and can be considered more reliable.
[e] For extended sources, estimates of the semi-major axes (S/N < 3 in brackets), otherwise "p" for point source.

Table 2. *Herschel*-SPIRE sources observed with ALMA in the G073.4−57.5 field.

ALMA field	SPIRE source	S_{350}[a] [mJy]	S_{350}/S_{250}[b]	S_{500}/S_{350}[c]	S_{1300}[d] [mJy]
1	1	83 ± 10	0.90 ± 0.21	0.78 ± 0.22	3.6 ± 0.5
2	3	64 ± 10	0.96 ± 0.31	1.07 ± 0.23[f]	3.6 ± 0.2
3	7	56 ± 10	1.35 ± 0.58	0.74 ± 0.33	2.1 ± 0.1
4	11	50 ± 10	0.67 ± 0.23*	1.36 ± 0.26[f]	1.9 ± 0.2
5	13	50 ± 10	0.87 ± 0.34	0.73 ± 0.37	0.6 ± 0.2
6	15	49 ± 10	1.12 ± 0.50	0.97 ± 0.32	1.6 ± 0.1
7	19	44 ± 10	1.32 ± 0.71	0.25 ± 1.04*	3.6 ± 0.4
8	25[e]	41 ± 10	0.68 ± 0.29*	0.31 ± 0.92*	0.5 ± 0.1

[a] 350-μm flux density of SPIRE sources in mJy. SPIRE source IDs 19 and 25 have uncertain detections at 500 μm.
[b/c] Colours of SPIRE sources. An asterisk (*) indicates sources not red enough to formally pass the criteria of Planck Collaboration et al. (2015), although they would within 1 σ.
[d] Integrated 233-GHz flux density of ALMA galaxies (i.e., summed over the values in bold font in Table 1) per *Herschel* source.
[e] This *Herschel* source lies outside the iso-surface-brightness contour encompassing 50 % of the *Planck* peak flux density at 545 GHz.
[f] The same 500-μm flux density was assigned to both SPIRE sources 3 and 11, instead of deblending the flux in the 500-μm image. If we split the 500-μm flux among to the two sources proportionally to their 350-μm flux, we obtain as S_{500}/S_{350} ratios 0.60 for both sources, instead of 1.07 and 1.36.

defined as [3.6] − [4.5] > −0.1 (in AB mag). Aperture photometry was performed in a 2″ radius circular aperture, and aperture corrections were applied. The catalogues were then cut to 50 % completeness in channel 2 (at 2.5 μJy). The surface density of IRAC red sources was computed in a circle of radius 1′ around SPIRE source ID 1 (which is the brightest red source in the *Herschel*-SPIRE field). The resulting surface density estimate is 14.6 arcmin^{-2}. When compared to the field value derived from the *Spitzer* Ultra Deep Survey (SpUDS) data at the same depth, which has a mean source density of 9.2 arcmin^{-2} (and a standard deviation of 2.2 arcmin^{-2}), this corresponds to an overdensity of approximately 2.5 σ (Martinache 2016).

The ALMA detections have a match in at least the channel 2 image (see Fig. 3), apart from galaxy ID 14, where there is emission in the *Spitzer* channel 2 map, but no significant enough detection. Most of them have a positional difference of $d < 0.4''$,

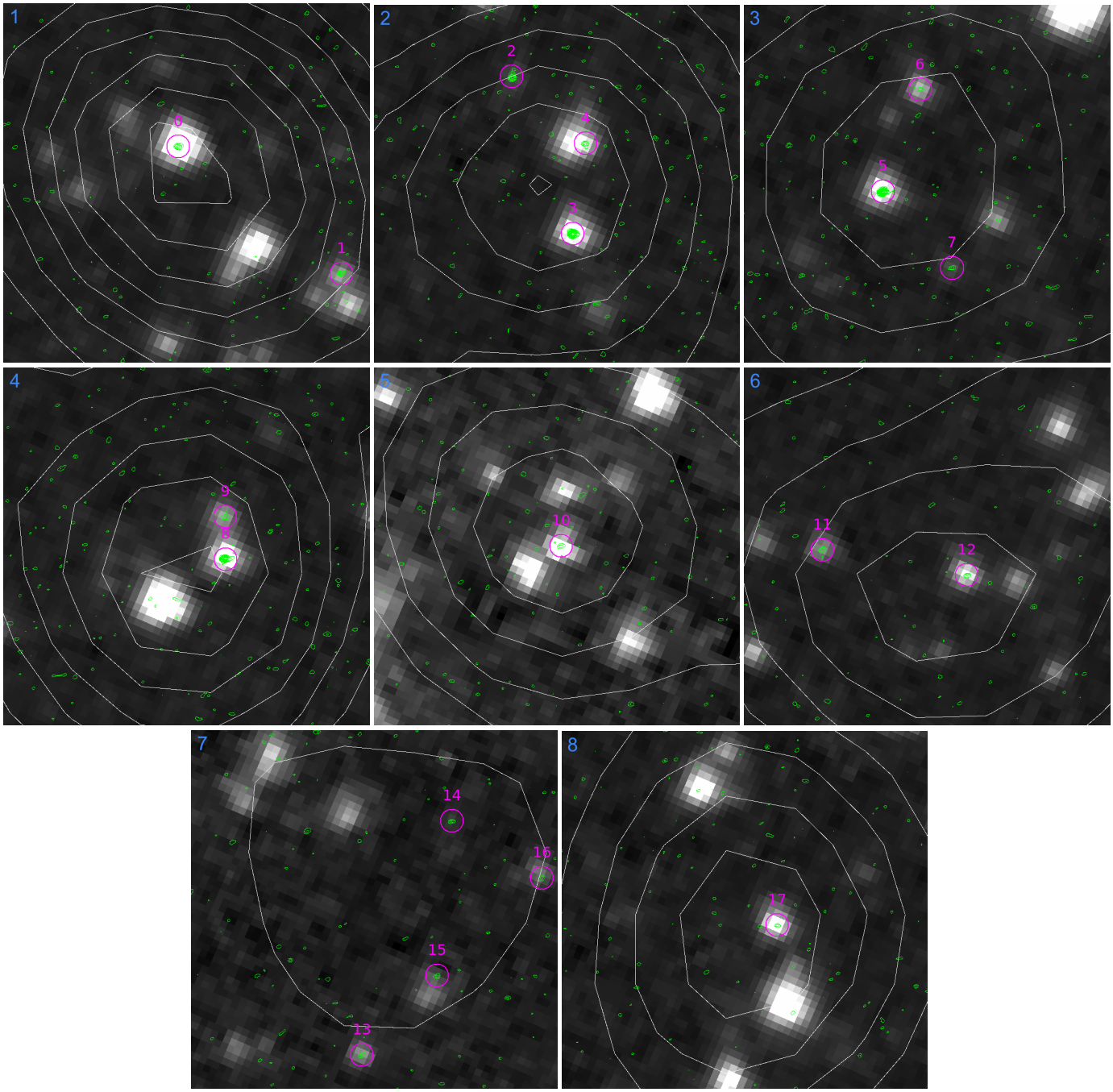

Fig. 3. *Spitzer* channel 2 postage stamps (30″ × 30″) in grey scale (from 0.35 to 0.6 MJy sr^{-1}) of the eight ALMA fields. White contours show the *Herschel* 250-μm surface brightness (from 0.01 Jy beam^{-1} in 0.005 Jy beam^{-1} or 1 σ steps). Green contours represent the ALMA surface brightness (from 0.12 mJy beam^{-1} in 0.06 mJy beam^{-1} or 1 σ steps). The detected ALMA sources are labelled with 1″ magenta circles; with the ALMA fields numbered in blue.

Table 3. SCUBA-2 sources in G073.4−57.5.

SCUBA-2 ID	RA [h:m:s]	Dec [d:m:s]	S_{850} [mJy]
0	23:14:42.3	−04:16:40	10.4 ± 1.8
1	23:14:42.6	−04:20:00	13.6 ± 2.5
2	23:14:41.8	−04:17:44	8.3 ± 2.0
3	23:14:34.6	−04:17:00	7.2 ± 1.8
4+	23:14:38.4	−04:16:25	7.1 ± 1.6
5+	23:14:40.2	−04:17:00	5.5 ± 1.7

except for three ALMA galaxies: ID 4 (0.6″); ID 16 (0.7″); and ID 15 (1.1″). In these cases the IRAC emission is seen to be extended (likely composites of two sources), with the ALMA source position still matching the detectable surface brightness of the IRAC source. We note that these three galaxies (IDs 4, 15, and 16) match to blue IRAC sources. Note, the significant counterparts for ALMA IDs 2 and 7 appear weak in contrast in Fig. 3.

Searching for a stellar bump sequence (Muzzin et al. 2013) in the colour-magnitude diagram (see Fig. 4) of sources lying in a circle of radius 1′ (balancing increasing numbers versus avoid-

ing confusion) around SPIRE source 11, we found a median colour of IRAC red sources in this circle of 0.14 mag, and a dispersion of 0.15 mag. Most ALMA matches exhibit distinctly redder colours, with a median of 0.27 mag ([3.6]–[4.5]), and a dispersion of 0.13 mag. Such colours are compatible with a $z \simeq 1.7$ structure (Papovich 2008), but the scatter is high.

Comparing the distributions shown in the right panel of Fig. 4, ALMA sources, IRAC sources around SPIRE source 11, and IRAC sources from the COSMOS field for reference, the Kolmogorov-Smirnov statistic gives values between 0.31 and 0.56 (the highest for ALMA versus COSMOS) with p-values less than 0.02 for ALMA versus IRAC and less than 2×10^{-5} relative to COSMOS, thus the differences in the distributions are large and significant.

4.5. CFHT WIRCam J and K

G073.4−57.5 was observed by CFHT-WIRCam at 1.3 μm (J band) and 2.1 μm (K_s band) in projects PID: 13BF12 and PID: 14BF08 (PI: H. Dole). The cumulated integration times were 9854 s and 4475 s for the J and K_s bands, respectively. The area covered was $25' \times 25'$, and the central $18' \times 19'$ was used for the analysis in order to exclude the edges with high noise. For the analysis we extracted sources using `SExtractor` in dual mode with detection in K_s band, reaching $K_{lim} = 22.94 \pm 0.01$ (AB, statistical error only) and $J_{lim} = 24.01 \pm 0.01$ at a threshold level of 2.5 σ (50 % completeness). The aperture photometry was performed in a 2″ radius circular aperture and we applied the aperture correction similarly as with the IRAC data. All sources with detection problems in the K_s band, flagged by `Sextractor`, were removed from the analysis. We then matched the resulting catalogue with the 18 *Spitzer*-IRAC + ALMA sources and found 13 matches within 0.6″, (consistent with the seeing of the CFHT data). The five unmatched sources are IDs 1 and 10 (best match separation > 2.5″), and 2, 7, and 14 (not detected in K_s).

In the JK colour-magnitude diagram (Fig. 5) we found the ALMA detected galaxies lying in the redder part of the overall distribution and mostly consistent with the expected colours (Franx et al. 2003) and sequence (Kodama et al. 1998) of a forming cluster at $z \simeq 2$. Combining the *Spitzer*-IRAC (Sec. 4.4) and CFHT-WIRCam colour information, we can compare the location of the ALMA galaxies with respect to evolutionary tracks of stellar population synthesis models (Bruzual & Charlot 2003). In Fig. 6 we summarise the evidence that the majority of ALMA sources lie at redshifts $z \simeq 2$ following the colour–redshift criteria of Papovich (2008) and Franx et al. (2003), and the evolutionary state predictions for a 1.4-Gyr-old simple stellar population (corresponding to a formation redshift $z_f = 3.5$ for an observed redshift of $z = 2$). The galaxies with ALMA IDs 3, 5, 6, 8, and 9 appear to be more consistent with a redshift below 2, whereas the colours of IDs 11, 12, 13, 15, and possibly 17 seem to indicate redshifts above 2, while having larger errors. ALMA IDs 0, 4, and 16 may be interlopers at lower redshift ($z \leq 1$).

VLT-HAWKI data, which are also available and consistent, have been used for Fig. 2 only.

4.6. WISE

Additional mid-IR data were obtained from the AllWISE catalogue (Wright et al. 2010; Mainzer et al. 2011) using a search radius of 3″. WISE counterparts in the W1 (3.4 μm) and W2 (4.5 μm) bands were found for six galaxies (ALMA IDs 0, 8, 9, 13, 15, and 16), and in W3 (12 μm) for one, ALMA ID 0.

4.7. Pan-STARRS

We also searched the Pan-STARRS (*grizy*) DR1 data[4] (Chambers et al. 2016), since even upper limits can provide additional contraints to the fits. The upper limits in AB mags are $g = 23.3$, $r = 23.2$, $i = 23.1$, $z = 22.3$, and $y = 21.4$.

4.8. VLA FIRST

A potential AGN contribution can be constrained from the low frequency radio maps at 1.4 GHz of the VLA FIRST Survey (Becker et al. 1995). We find no strong evidence of flux at the positions of the ALMA galaxies. The highest peak brightness of 0.62 mJy beam^{-1} is seen within the 5.4″ synthesized beam from the position of ALMA ID 12, and still below the 0.75 mJy threshold (5 σ) considered for significantly detected point sources.

5. Analysis

5.1. Source counts

Since we have targeted only the brightest *Herschel* sources found within this *Planck* peak, we can only make a qualitative comparison to known average ALMA mm source counts in order to discuss roughly how overdense in sources these regions are.

Each ALMA field has been searched for sources within a 37″ diameter circle, over which the noise increases from the centre outwards by up to a factor of 5. The area of each field is 0.30 arcmin^2, and adding together the eight fields we obtain a total survey area of 2.4 arcmin^2, or 6.6×10^{-4} deg^2. For the count estimate we take the eight sources in our sample with flux densities > 0.9 mJy. The effective area over which these sources can be detected is 75 % of the total area (i.e., where rms < S_ν / S/N = 0.9 mJy / 4.5 = 0.2 mJy). Thus, the counts are 8 / (0.75 $\times$ 6.6×10^{-4} deg^2) = 1.6×10^4 deg^{-2}.

Comparing to recent blank-field counts of ALMA sources (e.g., Hatsukade et al. 2016; Dunlop et al. 2017), serendipitous counts derived from various archival data (e.g., Hatsukade et al. 2013; Ono et al. 2014; Carniani et al. 2015; Oteo et al. 2016; Fujimoto et al. 2016), or source numbers found in lensing cluster fields (e.g., González-López et al. 2016), we estimate an expected 1.2-mm source density of 0.6–2 $\times$ 10^3 deg^{-2}, where the lower estimate (from Oteo et al. 2016) was derived from a relatively large area of different fields used for the serendipitous searches, which might be expected to reach beyond the effects of cosmic variance. Thus, the number of sources we found in the ALMA pointings of G073.4−57.5 is a factor of 8–30 higher than estimates of the average number of mm sources in the sky.

It is also interesting to examine the total number of mm/submm sources found in G073.4−57.5 so far, namely 18 from ALMA, even without a complete mosaic of the total emission region of the *Planck*/*Herschel* peak, and an additional four from SCUBA-2, for a total of 22 mm/submm sources in the area of the *Planck* peak. In comparison, typical "proto-cluster" overdensities, not selected by their high integrated submm flux, do not show the same abundance. Examples include the COSMOS $z = 2.47$ structure (Casey et al. 2013, 2015) and the SSA22

[4] https://panstarrs.stsci.edu

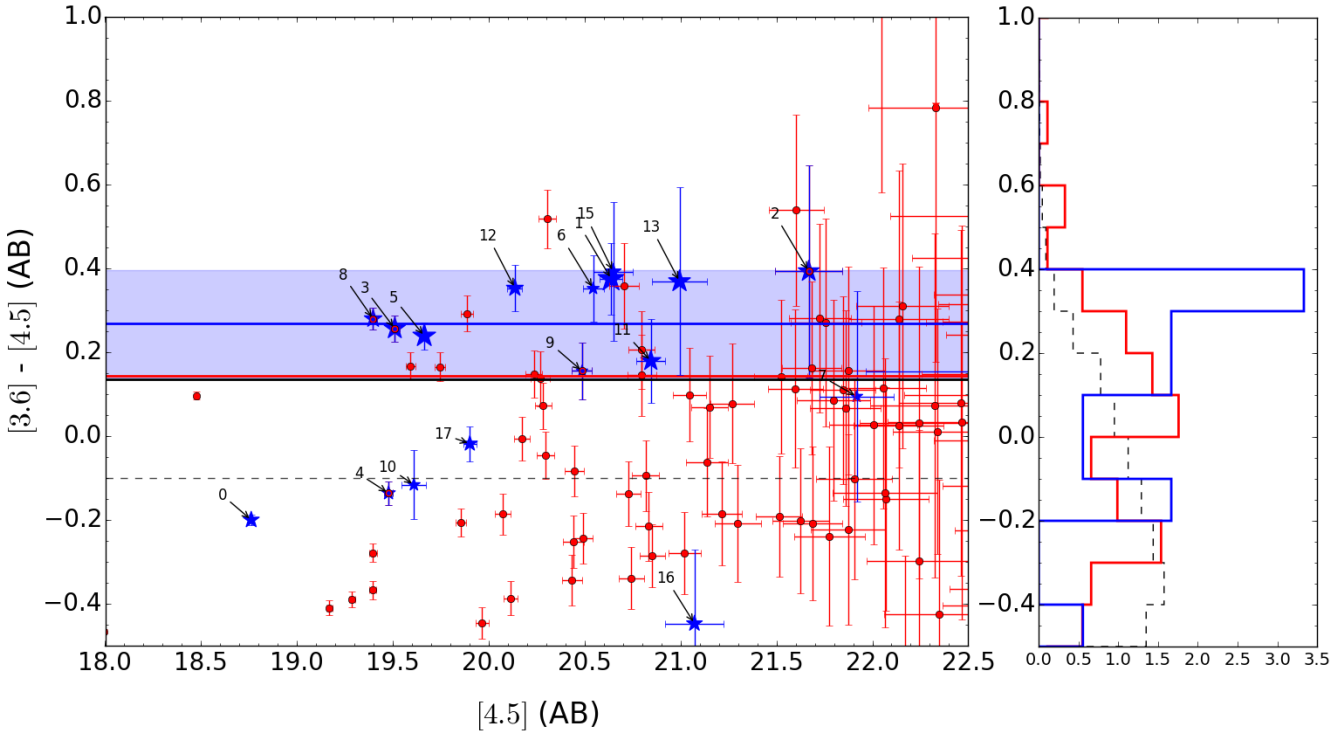

Fig. 4. *Left*: Colour ([3.6] − [4.5]) versus magnitude ([4.5]) diagram for IRAC sources (red points) located within 1′ of SPIRE source 11, and for all the ALMA sources (blue stars). Numbers indicate the ALMA source IDs, as in Table 1. The black dashed line indicates a colour of −0.1 (red sources are defined to have colours above this value), the red line indicates the median colour of IRAC red sources within 1′ of SPIRE source 11 (0.14 mag), the blue line indicates the median colour for the ALMA sources matched to IRAC red sources (0.27 mag). The dispersions around these medians are 0.15 and 0.13, respectively (the latter is indicated by the blue region). The solid black line indicates the colour of a single stellar population formed at $z_f = 5$, passively evolved to redshift $z = 1.5$ (from Bruzual & Charlot 2003), but note that extinction and possible metallicity effects have not been considered. Most ALMA sources lie on a sequence in this colour-magnitude plane, a characteristic feature of high-z structures (e.g., Muzzin et al. 2013; Rettura et al. 2014). Note that ALMA ID 14 is not plotted here, because it was not detected in the *Spitzer*-IRAC data. *Right*: Normalized distribution of the colour of IRAC sources: the red line corresponds to sources within 1′ of SPIRE source 11, the blue line shows the ALMA sources, and the black dashed line shows the distribution of the colours of general sources in the COSMOS field for comparison. There is a significant excess of red galaxies around SPIRE source 11, in particular for the ALMA detections (see text for details).

$z = 3.09$ structure (Umehata et al. 2015), each of which contains 12 sources (see Casey 2016, in particular their table 1, for a comprehensive summary of star-forming galaxies in several overdense regions) at a comparable depth (although the SCUBA-2 850-μm data on the COSMOS structure are not as deep at 0.8 mJy rms, see Casey et al. 2013). In a more recent study of the SSA22 structure, Umehata et al. (2017) found 18 ALMA sources ($> 5\,\sigma$) at 1.1mm, but over an area of $2' \times 3'$ and with a depth of 0.06–0.1 mJy, much wider and overall somewhat deeper (given their shorter wavelength and homogeneous coverage) than our data, consisting of approximately 16 times our on-source time with comparable numbers of antennas and conditions. At similar depth and area to our selected eight pointings, this would correspond to about four detections. A comparison with the $z = 1.46$ cluster XCS J2215.9−1738 studied by Stach et al. (2017) with the same ALMA on-source time in a 1 arcmin^2 central mosaic shows a similar number of sources (14, with 12 likely members), but they are all weaker (< 1 mJy). They find a total SFR of 850 $M_\odot\,yr^{-1}$, which is lower than the 2060 $M_\odot\,yr^{-1}$ in our sample (see below). The SCUBA-2 sources in XCS J2215.9−1738 break up mostly into groups of two to three ALMA sources, similar to the SCUBA-2 and *Herschel* sources in G073.4−57.5.

We can conclude that for our data contamination by the average background sources is expected to be small, about 1–3 galaxies not related to the cause of the *Planck* peak should be present in the data. We discuss later whether gravitational lensing could affect the number counts.

5.2. Spectral energy distributions and photometric redshifts

The detection, in most cases, of several ALMA galaxies (with sub-arcsecond accuracy) per single *Herschel* target allows us to employ a deblending technique to estimate the *Herschel*-SPIRE fluxes of these galaxies, which can then be used to fit SEDs and derive several physical properties. To accomplish this we used a combination of a recently developed algorithm called `SEDeblend` (MacKenzie et al. 2017), specifically designed for confused FIR imaging, and `Hyper-z` (Bolzonella et al. 2000), which matches wider multi-wavelength coverage data to a library of galaxy templates.

We first apply `Hyper-z` to all available flux measurements for each source (excluding those from *Herschel*-SPIRE, which are initially too confused to be useful) to obtain posterior prob-

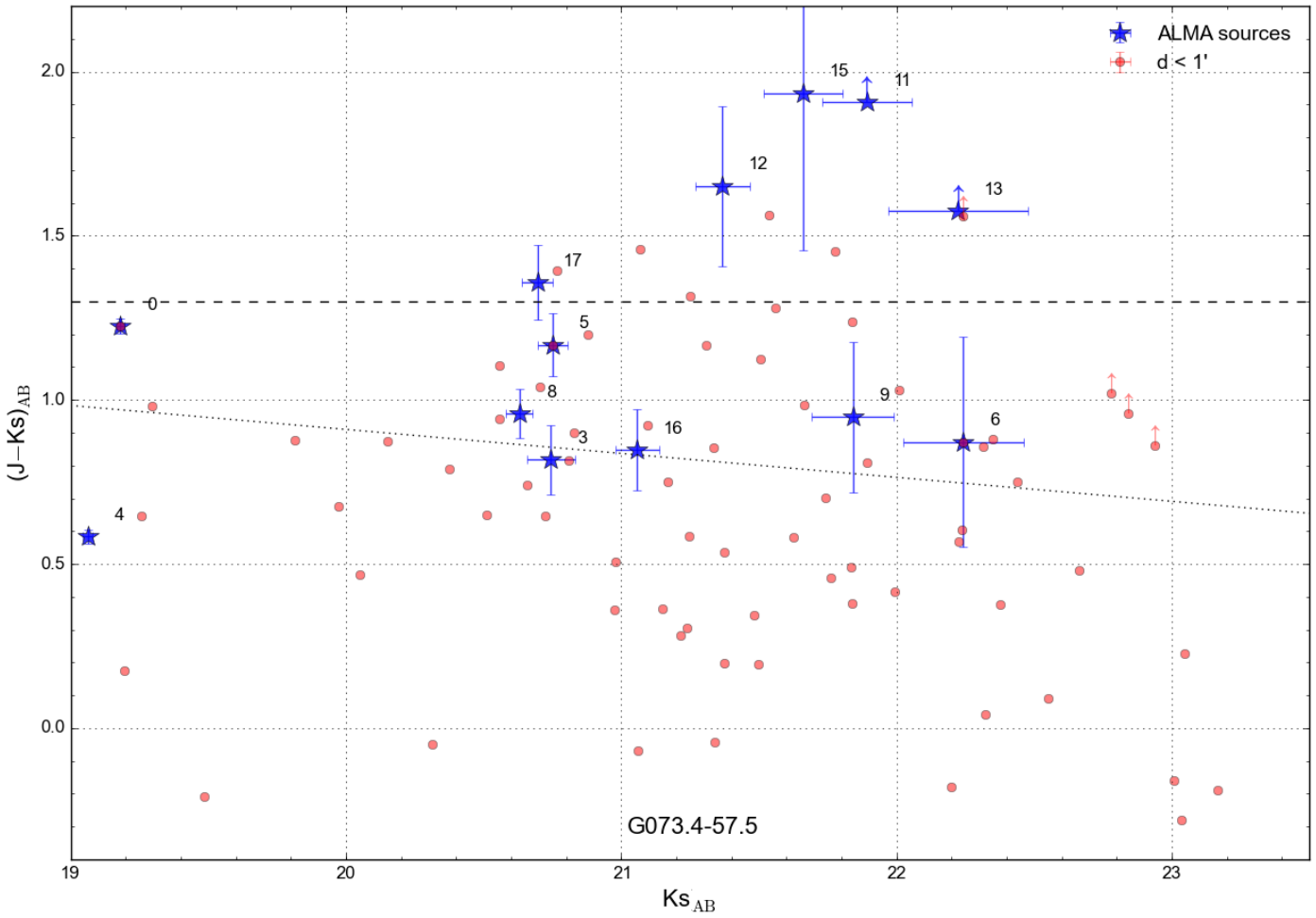

Fig. 5. Colour- ($J - K_s$) magnitude (K_s) diagram for the ALMA-detected sources (in blue) versus other sources (in red), the latter within 1′ of SPIRE ID 1; the dashed line indicates a colour of 1.3 (the Franx et al. 2003 criterion for the colour of galaxies at $z \simeq 2$). Sources with ALMA IDs 1, 2, 7, 10, and 14 are not plotted because they are not detected in the NIR. The dotted line shows the red sequence of the Coma cluster passively evolved back in time to $z = 1.5$ (Kodama et al. 1998). ALMA galaxies are in the redder part of the colour distribution, and are consistent with the sequence of a forming cluster at $z \simeq 1.5$.

ability distributions for photometric redshifts. For the 850-μm data from SCUBA-2, the flux density from SCUBA-2 ID 4+ was assigned proportionally to the ALMA flux of IDs 2 and 4 (ID 3 also falls in field 2, but is 11″ from the SCUBA-2 position, see Fig. 2), and the 850-μm flux density from SCUBA2-ID 5+ was assigned proportionally to ALMA IDs 8 and 9. Similarly, the *Herschel*-SPIRE flux densities were initially assigned with the ALMA flux density ratios of the constituent galaxies, giving results consistent with excluding *Herschel*-SPIRE data. The library of SED templates used covers the full optical-mm spectral range (Polletta et al. 2007; Berta et al. 2013); furthermore, three templates were added, obtained from fitting the average, the bright, and the faint stacked SEDs of the ALESS sample (da Cunha et al. 2015) using `MAGPHYS`.

We then used the resulting photometric redshift posterior probability distributions as inputs to `SEDeblend`. To summarize briefly, `SEDeblend` reconstructs the *Herschel*-SPIRE 250-μm, 350-μm, and 500-μm images and the SCUBA-2 850-μm image by placing a point source multiplied by the appropriate instrumental point spread function at each location of a detected ALMA galaxy and adding a constant background offset, then uses a Markov chain technique to simultaneously fit for galaxy SED parameters. The ALMA images are not reconstructed, since the much greater angular resolution there, after `CLEAN`ing, leads to essentially no source blending. The model takes into account each *Herschel*-SPIRE instrumental transmission function (typically amounting to a 10 % flux correction), and considers calibration uncertainties by multiplying the flux in each band by a nuisance parameter, whose prior is a Gaussian function with a mean of 1.0 and a standard deviation given by each instrument's quoted calibration uncertainty. The SEDs are modelled as modified blackbodies (Eq. 1) at a redshift z with a temperature T_d, an overall normalization constant, and the dust emissivity index is fixed at $\beta = 2.0$. For more details on `SEDeblend` we refer the reader to MacKenzie et al. (2017).

For the fitting, a Markov chain Monte Carlo (MCMC) algorithm with Gibbs sampling and adaptive step-sizing is used to maximize a Gaussian likelihood function calculated pixel-by-pixel for the SPIRE and SCUBA-2 images, and source-by-source for the ALMA flux measurements. The chain is run for 120,000 iterations and the first 20,000 iterations are removed as the "burn-in" sequence. We set a sufficiently wide uniform prior on the amplitudes of the modified blackbody SEDs and the background levels to leave them effectively unconstrained, and a uniform prior between 10 and 100 K on the dust temperatures (since no galaxies have been observed to lie outside this

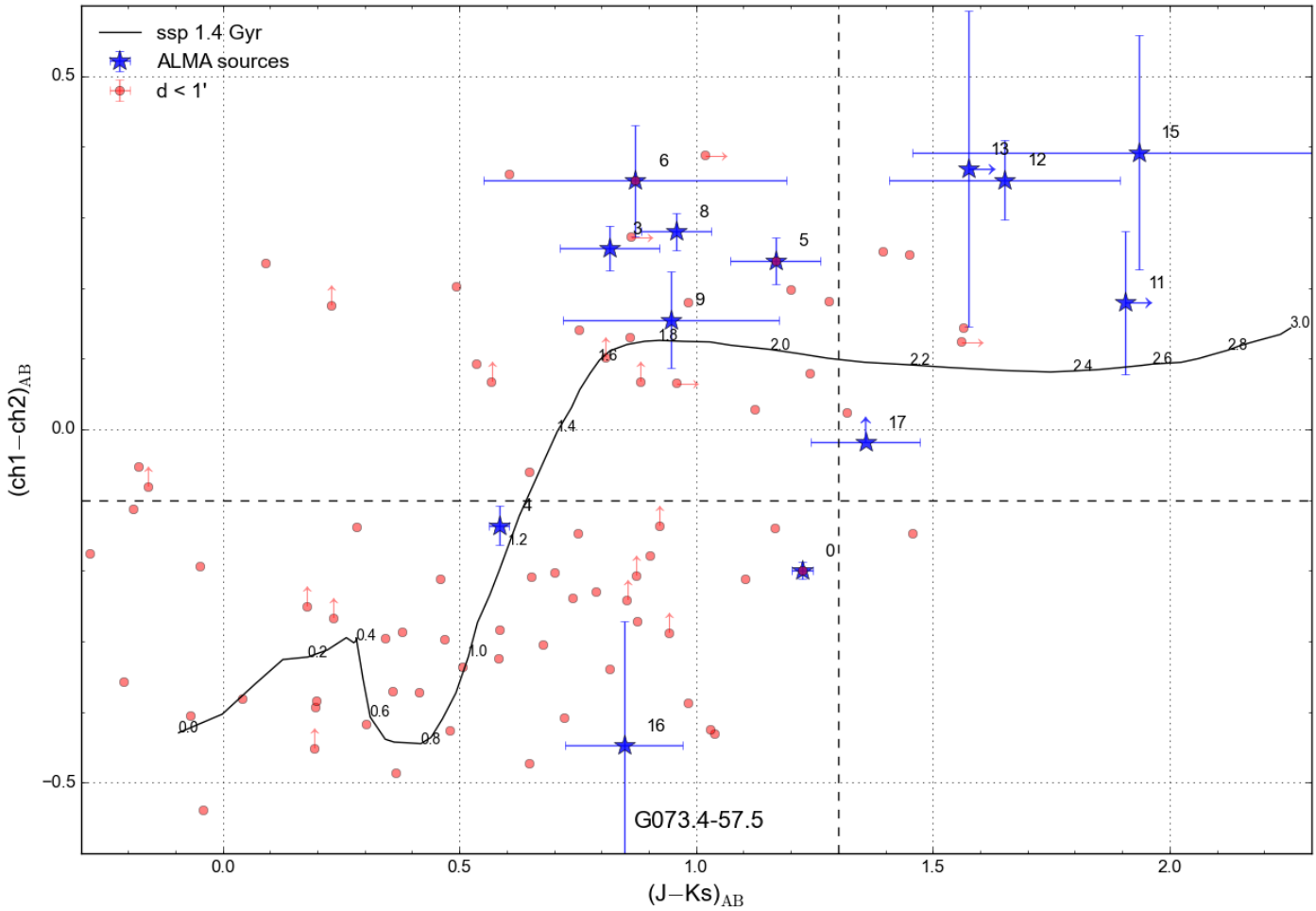

Fig. 6. *Spitzer*-IRAC versus CFHT WIRCam colour-colour diagram with a track drawn from Bruzual & Charlot (2003) for a 1.4-Gyr-old simple stellar population, numbered by redshift. The horizontal and vertical dashed lines indicate the Papovich (2008) and Franx et al. (2003) criteria, respectively, representing colours of $z \simeq 1.3$ and $z \simeq 2$ galaxies (cf. the labels on the model curve, also). A redshift around $z = 1.6$–2.6 is indicated for the majority of the ALMA galaxies. Arrows indicate $2\,\sigma$ limits for the sources not detected in any channel or band.

range, e.g., Dale et al. 2012; Swinbank et al. 2014). To remove the degeneracy between temperature and redshift in the modified blackbody model, the photometric redshift posterior probability distribution from `Hyper`-z in the previous step is inputed as the prior for the new photometric redshift.

From the resulting Markov chain we derive the *Herschel*-SPIRE flux densities in each band by evaluating $S_\nu(\nu_b)$, with b labelling the band, from each iteration within the MCMC algorithm as marginal likelihoods, and report them in Table 4, along with 68 % confidence intervals. For IDs 11, 15, and 16 the 68 % confidence interval extends to 0 mJy, thus we assign upper limits only. For consistency, we checked the mm/submm properties (such as dust temperature, FIR luminosity, and SFR, discussed in the following section) derived from `SEDeblend` with those derived in Section 5.3 and found them to be in generally good agreement.

We lastly re-ran `Hyper`-z with the now deblended *Herschel*-SPIRE and SCUBA-2 flux densities included. The best-fit templates and SEDs are shown in Fig. A.1 in the Appendix, and photometric redshifts and associated uncertainties are listed in Table 5. The redshift uncertainties correspond to the range of redshifts with a probability higher than half the maximum value.

Table 4. Deblended *Herschel*-SPIRE flux densities for the individual ALMA detected galaxies.

ALMA ID (field)	S_{250} [mJy]	S_{350} [mJy]	S_{500} [mJy]
0 (1b)	71^{+3}_{-4}	48^{+2}_{-2}	22^{+1}_{-1}
1 (1a)	19^{+3}_{-2}	29^{+1}_{-3}	23^{+1}_{-2}
2 (2b)	5^{+2}_{-2}	10^{+3}_{-2}	10^{+1}_{-1}
3 (2a)	25^{+3}_{-5}	25^{+3}_{-2}	$16^{+1.4}_{-0.9}$
4 (2c)	31^{+5}_{-3}	16^{+2}_{-3}	6^{+1}_{-1}
5 (3a)	21^{+4}_{-4}	25^{+2}_{-3}	17^{+1}_{-2}
6 (3c)	14^{+3}_{-4}	11^{+2}_{-2}	$5.8^{+0.8}_{-0.8}$
7 (3b)	9^{+4}_{-3}	9^{+2}_{-2}	$5.0^{+1.0}_{-0.9}$
8 (4a)	64^{+4}_{-4}	43^{+3}_{-2}	20^{+2}_{-1}
9 (4b)	3^{+2}_{-2}	6^{+2}_{-2}	7^{+1}_{-2}
10 (5a)	46^{+4}_{-3}	34^{+3}_{-2}	17^{+1}_{-2}
11 (6a)	< 11	< 14	< 9
12 (6b)	28^{+4}_{-2}	22^{+2}_{-2}	$11.6^{+1.0}_{-0.7}$
13 (7a)	9^{+4}_{-2}	16^{+3}_{-3}	14^{+1}_{-2}
14 (7b)	18^{+3}_{-3}	18^{+2}_{-3}	10^{+1}_{-1}
15 (7c)	< 0.5	< 2	< 3
16 (7d)	< 0.5	< 2	< 3
17 (8a)	40^{+3}_{-3}	24^{+2}_{-2}	$9.8^{+1.0}_{-0.9}$

Reasonably good fits (median $\chi^2_{\rm red} = 0.64$) are obtained for most of the galaxies, with the exception of ID 15 and 16, where the template overestimates the observed mm/submm fluxes. For these sources, which are found in ALMA region 7, it seems plausible that the source blending is simply too substantial to be overcome; four galaxies are sharing a combined flux half that of most of the other regions, where there are three or fewer galaxies. We thus caution interpretation of galaxies 13 through 16.

Note, that the two galaxies within region 4, IDs 8 and 9, are the most closely-spaced pair in the data, separated by less than a pixel in the SPIRE maps. This leads to strong degeneracies between the best-fit SED parameters found by `SEDeblend` for these two galaxies, which may result in unreliable flux estimates. However, the redshift of $z \simeq 1.5$ our procedure associates with galaxy 8 seems to agree with the ALMA CO spectroscopic redshift (see Sect. 6 for details).

We validate our photometric redshifts by first checking the SCUBA-2 flux density predicted for all ALMA galaxies based on the fits. We find that our best-fit SEDs give a total SCUBA-2 flux of 61 mJy, in good agreement with the stacking result of (56 ± 11) mJy. Next, since an extension of `Hyper-`z into the millimetre regime is not commonly done, we compare our photometric redshifts to fits carried out with the `EAZY` code (Brammer et al. 2008) using only NIR (J, K, [3.6], [4.5]) data, which uses a different set of templates. We show a comparison of the two results in Fig. 7, with the agreement being consistent within the uncertainties for both of the methods.

5.3. FIR-derived parameters

From the best-fit SEDs we are able to derive IR luminosities, SFRs, dust masses, and stellar masses. The IR luminosities are calculated from the fits by integration from 8 to 1000 μm:

$$L_{\rm IR} = \frac{4\pi D_{\rm L}^2}{1+z} \int_{c/1000}^{c/8} S_\nu(\nu_{\rm e}/(1+z))\, d\nu_{\rm e}. \quad (3)$$

SFR estimates are derived by assuming the relationship in Kennicutt (1998), modified for a Chabrier IMF (Chabrier 2003), i.e., SFR[$M_\odot$ yr^{-1}] = 9.5×10^{-11} $L_{\rm IR}$[$L_\odot$]. In order to estimate stellar masses we fit only the WIRCam-IRAC SED, fixing the redshift to the photometric redshift, using `Hyper-`z and the composite stellar population models from Bruzual & Charlot (2003), and assuming a Chabrier IMF. The dust masses are calculated here following Eq. (2). The best-fit parameters, along with the dust masses, are listed in Table 5. The dust temperatures with an average of $\langle T_{\rm d}\rangle = 24.9$ K are low, but not out of the range that can be expected for normal galaxies at $z \gtrsim 1$. The dust masses are within the expected range of 10^8–10^9 $M_\odot$.

5.4. Relationship to main-sequence galaxies

Half of the ALMA galaxies are classified as ULIRGs (L(IR) ≥ 10^{12} $L_\odot$), with SFRs consistent with those observed in starbursting galaxies. The highest SFR (> 300 $M_\odot$ yr^{-1}) is measured in ID 8 ($z_{\rm CO} = 1.54491$, see Section 6), and (≥ 150 $M_\odot$ yr^{-1}) in IDs 1 ($z_{\rm phot} = 2.19^{+0.15}_{-0.12}$), 11 ($z_{\rm phot}$ = 1.1–4.0), 12 ($z_{\rm phot} = 1.51^{+0.27}_{-0.17}$), 13 ($z_{\rm phot}$ = 1.7–4.0), and 17 ($z_{\rm phot} = 1.17^{+0.08}_{-0.09}$), although as described in the previous section, the fit for galaxy 13, as well as the other galaxies in ALMA region 7, may be unreliable.

In Fig. 8, we compare the derived stellar masses with the M^* values in the Schechter function obtained by fitting the mass function of star-forming galaxies in the redshift ranges 0.2–0.5, 0.5–0.8, 0.8–1.1, 1.1–1.5, 1.5–2.0, 2.0–2.5, 2.5–3.0, 3.0–3.5, and 3.5–4.0 (Davidzon et al. 2017). The ALMA galaxies have stellar masses comparable with the predicted M^* values, albeit with a considerable spread and two outliers with significantly lower M^* values. 9/18 (50 %) of the galaxies have stellar masses higher than M^*, they range from 6 × 10^{10} to 2 × 10^{11} $M_\odot$, so they are already quite massive. Note, that the most massive galaxies are on the MS, or below it, suggesting that they are perhaps on the verge of quenching. ALMA galaxy ID 8 is an exception in this respect.

In Fig. 9 we plot the IR-derived SFR divided by the expected SFR based on the main sequence (MS) at the source redshift, as parameterized by Speagle et al. (2014) (i.e., the "starburstiness"), as a function of redshift. This figure shows that 13 of our ALMA galaxies (72 %) lie within a factor of 3 of the main sequence (shown by the grey region), while two ALMA galaxies lie below this region (IDs 15 and 16) and three lie above (IDs 1, 8, and 14). These latter three sources (where it must be noted that ID 14 may not be reliable) are thus experiencing an enhanced star-forming activity, consistent with being starburst galaxies. Interestingly, four galaxies at $z \simeq 1.5$ are very close to the main sequence, again ID 8 is an exception. It is also interesting to note that there is another group of four galaxies (IDs 1, 2, 7, and 13) with similar, in this case larger starburstiness (about a factor 3 above the MS value) that lie at $z_{\rm photo} \simeq 2.2$–2.7, and thus could also be at the same redshift as each other.

In Fig. 10 we show the SFRs as a function of M_*. The expected range for MS galaxies at redshift $z \simeq 1.5$ (Speagle et al. 2014) is also shown, along with a region indicating a spread of a factor of 3. Starburst galaxies are typically offset from the MS towards SFRs that are around 3 times higher. IDs 1, 8, in particular, satisfy this criterion.

6. Serendipitous line detections

6.1. ALMA galaxies ID 3 and 8

Spectral cubes of the ALMA primary beam convolved continuum (128 channels for each of the 4× 2-GHz wide spectral windows) were made for the eight fields with a spectral binning of width 0.08 GHz giving 25 frames. Fluxes quoted in the text are beam corrected.

ALMA galaxy ID 3, the brightest mm galaxy located in ALMA field 2, shows the detection of a strong line at 226.54 GHz (see line peak in Fig. 11 top panel). We found an integrated flux density of (2.5 ± 0.2) Jy km s^{-1} beam^{-1} at the spatial peak, and (2.9 ± 0.2) Jy km s^{-1} in an extended aperture, with a line width of (370 ± 40) km s^{-1}, for the FWHM in the Gaussian fit. With the physical size of this source derived from Table 1, the dynamical mass is $M_{\rm dyn} = 2.2 \times 10^{11}$ $M_\odot$ = (400 km s^{-1})^2 × 5.9 kpc / G, as compared to a stellar mass of $M_* = 1.2 \times 10^{11}$ $M_\odot$ (from Table 5).

The galaxy shows a smooth velocity gradient from north-east to south-west (see Fig. 12 middle panel), but it is spatially only barely resolved. CO transitions are known to be bright for mm and submm galaxies (e.g., Carilli & Walter 2013; Vieira et al. 2013), and would correspond to the redshifts z = 1.035 CO(4–3), 1.544 for CO(5–4), 2.052 for CO(6–5), and 2.561 for CO(7–6), keeping with the most plausible range of $z \simeq$1–3.

While associating the observed lines with the CO(5–4) or CO(6–5) transitions appears the most plausible conclusion (since it provides the closest match for the photometric redshift of ALMA galaxy ID 3 and all the higher redshift galaxies appear to cluster around $z \simeq$ 1.5–2), we briefly discuss other interpre-

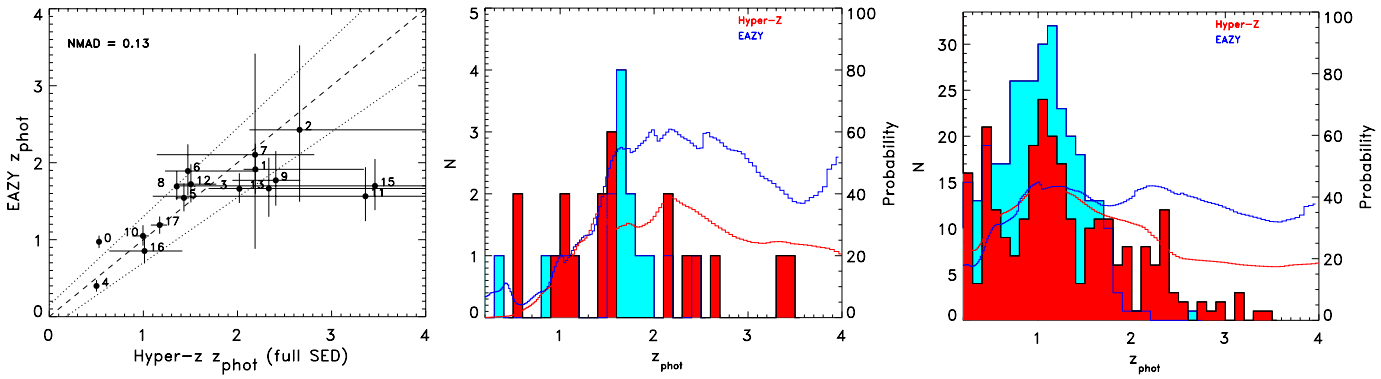

Fig. 7. *Left*: Redshift comparison. The combined probability density functions for the photo-z (`EAZY` [blue] / `Hyper`-z [red]) results of all ALMA galaxies shown as curves in this plot have been derived as the average from the individual probability density functions for each galaxy. The histograms show the distributions of the peak probabilities for the two methods. `EAZY` shows a clear concentration, consistent with z=1.54 and interlopers around and below $z \simeq 1$. `Hyper`-z also shows some disagreement with a few more galaxies at and above $z \simeq 2$. *Middle panel:* Comparison between the estimates for photometric redshift fitting with `Hyper`-z (x-axis), using all (NIR+FIR) data, and with `EAZY` (y-axis), using only NIR data. The agreement is satisfactory within the overall uncertainties of the methods. The dotted lines expresses ±15 % deviations around the equality relation (dashed line), i.e., $|z_{\rm hz} - z_{\rm ez}|/(1 + z_{\rm ez}) = 0.15$. A separation into two groups at higher and lower redshifts is apparent. As described in the text, the redshift groups are clustered, but mixed with respect to the eight *Herschel* sources. *Right*: Same as middle panel but for all NIR sources in the G073.4−57.5 field. In contrast to the ALMA detected galaxies the $z \simeq 1$ probability peak is the dominant feature.

Table 5. Best-fit SED parameters. Peaks of the probability distributions are given between the percentiles defining the 15.9 % to 84.1 % range.

ID	$z_{\rm phot}$	$\log(L_{\rm IR})^a$	$\mathrm{SFR}^b_{\rm IR}$	$T_{\rm dust}$	$\log(M_{\rm dust})$	$\log(M_*)^c$
		[$L_\odot$]	[$M_\odot$/yr]	[K]	[$M_\odot$]	[$M_\odot$]
0	(0.53) 0.53 (0.53)	(11.48) 11.53 (11.57)	(29) 32 (35)	(19.1) 19.8 (20.4)	(8.55) 8.58 (8.62)	(11.26) 11.27 (11.27)
1	(2.07) 2.19 (3.34)	(12.40) 12.42 (12.45)	(237) 251 (268)	(24.5) 25.2 (25.9)	(9.16) 9.19 (9.23)	(10.46) 10.48 (10.59)
2	(2.13) 2.66 (4.04)	(12.12) 12.13 (12.20)	(124) 129 (149)	(23.8) 24.5 (26.0)	(8.95) 9.03 (9.08)	(10.06) 10.13 (10.77)
3	(1.37) 1.42 (1.46)	(12.01) 12.06 (12.12)	(96) 108 (125)	(21.9) 22.8 (23.9)	(8.92) 8.98 (9.03)	(11.04) 11.08 (11.15)
4	(0.50) 0.50 (0.51)	(11.01) 11.18 (11.38)	(10) 14 (23)	(19.5) 22.0 (25.2)	(7.84) 7.97 (8.08)	(9.92) 9.96 (10.02)
5	(1.34) 1.43 (1.49)	(11.95) 11.99 (12.04)	(85) 93 (105)	(21.5) 22.2 (23.0)	(8.92) 8.96 (9.00)	(11.00) 11.05 (11.21)
6	(1.23) 1.47 (2.22)	(11.79) 11.90 (12.02)	(59) 75 (100)	(26.9) 29.0 (31.6)	(8.13) 8.22 (8.30)	(10.77) 10.98 (11.06)
7	(1.14) 2.19 (2.82)	(12.02) 12.09 (12.22)	(99) 117 (159)	(31.2) 33.2 (36.4)	(8.08) 8.18 (8.26)	(9.86) 10.14 (10.63)
8	(1.56) 1.65 (1.67)	(12.55) 12.60 (12.65)	(337) 379 (427)	(30.7) 31.9 (33.2)	(8.65) 8.70 (8.74)	(10.70) 10.76 (11.14)
9	(1.95) 2.41 (2.67)	(11.85) 11.84 (11.93)	(68) 66 (80)	(23.7) 23.7 (25.3)	(8.72) 8.78 (8.80)	(10.66) 10.82 (11.32)
10	(0.88) 1.00 (1.06)	(11.93) 11.97 (12.01)	(81) 89 (98)	(23.3) 23.9 (24.5)	(8.66) 8.68 (8.70)	(10.85) 10.89 (10.91)
11	(1.10) 3.36 (4.04)	(12.07) 12.27 (12.47)	(112) 175 (277)	(27.1) 31.2 (35.7)	(8.50) 8.65 (8.80)	(11.32) 11.42 (11.45)
12	(1.34) 1.51 (1.78)	(12.16) 12.21 (12.26)	(136) 153 (174)	(28.1) 29.2 (30.5)	(8.47) 8.51 (8.56)	(11.03) 11.19 (11.25)
13	(1.69) 2.33 (4.04)	(12.18) 12.21 (12.27)	(145) 155 (176)	(23.7) 24.8 (26.2)	(8.96) 9.05 (9.12)	(10.30) 10.37 (10.82)
14	(0.79) 1.05 (2.49)	(11.52) 11.58 (11.65)	(31) 36 (42)	(19.8) 20.8 (21.9)	(8.58) 8.64 (8.69)	(8.50) 9.36 (9.88)
15	(1.39) 3.46 (4.04)	(11.40) 11.50 (11.57)	(234) 30 (36)	(19.6) 22.2 (24.5)	(8.55) 8.73 (8.92)	(10.92) 11.47 (11.57)
16	(0.64) 1.01 (1.41)	(10.20) 10.11 (10.13)	(1) 1 (1)	(10.0) 10.0 (11.6)	(8.53) 8.84 (8.93)	(9.74) 9.82 (10.71)
17	(1.08) 1.17 (1.25)	(12.13) 12.22 (12.30)	(128) 156 (190)	(29.6) 31.4 (33.3)	(8.22) 8.28 (8.35)	(10.78) 10.87 (11.09)

[a] 8–1000 μm (rest) luminosity derived by fitting the FIR SED with a single temperature modified blackbody model.
[b] SFR derived from $L_{\rm IR}$, assuming the relationship in Kennicutt (1998) modified for a Chabrier IMF, i.e., $\mathrm{SFR}[M_\odot\,\mathrm{yr}^{-1}] = 9.5{\times}10^{-11}\,L_{\rm IR}[L_\odot]$.
[c] Stellar mass derived from fitting the WIRCam-IRAC SED with the models of Bruzual & Charlot (2003).

tations. The higher redshift transitions ($J > 6$, corresponding to $z > 2.5$) would yield poorer agreement with the photometric redshifts, and in addition may be expected to be much weaker. The C I line would provide a direct identification, as its rest frequency of 809.34 GHz is very close to the rest frequency of the CO(7–6) line, which has a rest frequency of 806.65 GHz; however, this is not possible with our observation, since the expected 227.1-GHz (sky frequency) line would be inside the sideband

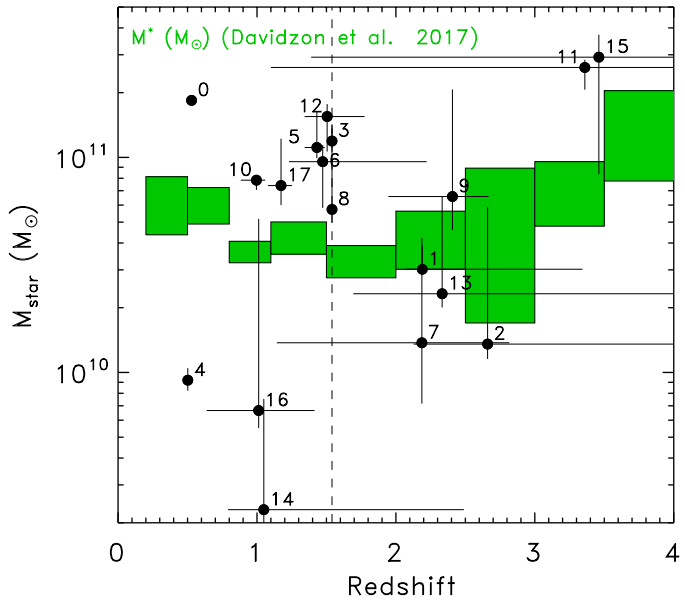

Fig. 8. Stellar mass as a function of photometric redshift for the 18 ALMA galaxies (full circles). The green rectangles represent the M^* values and their uncertainties obtained by fitting the mass function of star-forming galaxies in the redshift ranges 0.2–0.5, 0.5–0.8, 0.8–1.1, 1.1–1.5, 1.5–2.0, 2.0–2.5, 2.5–3.0, 3.0–3.5, and 3.5–4.0 with a Schechter function (Davidzon et al. 2017). The source IDs are labelled next to the corresponding symbols.

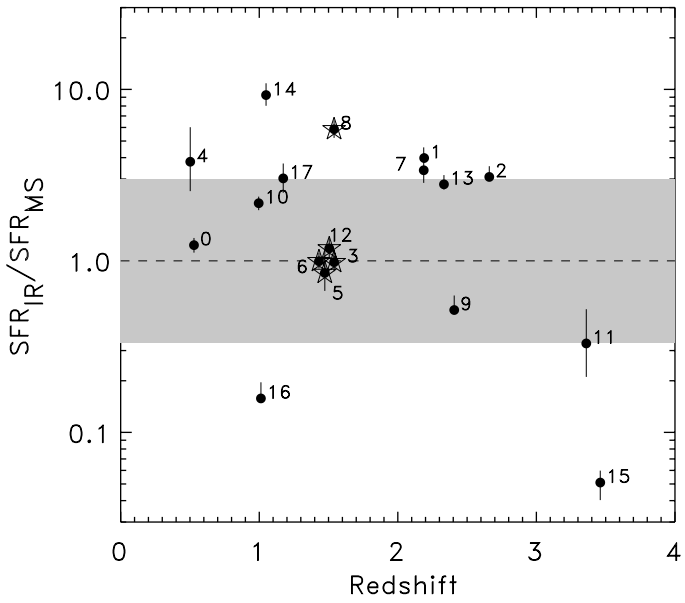

Fig. 9. "Starburstiness," which is the ratio of the star-formation rate to the SFR expected for the main sequence (using the relation at the respective redshift), plotted against redshift. A factor of 3 around the MS is indicated by the grey region. Stars indicate galaxies assumed to be at $z \simeq 1.54$.

separation. Moreover, a redshift around $z \simeq 1$ does not seem consistent with the colour and photo-z results of most galaxies, apart from those galaxies quite firmly identified as interlopers.

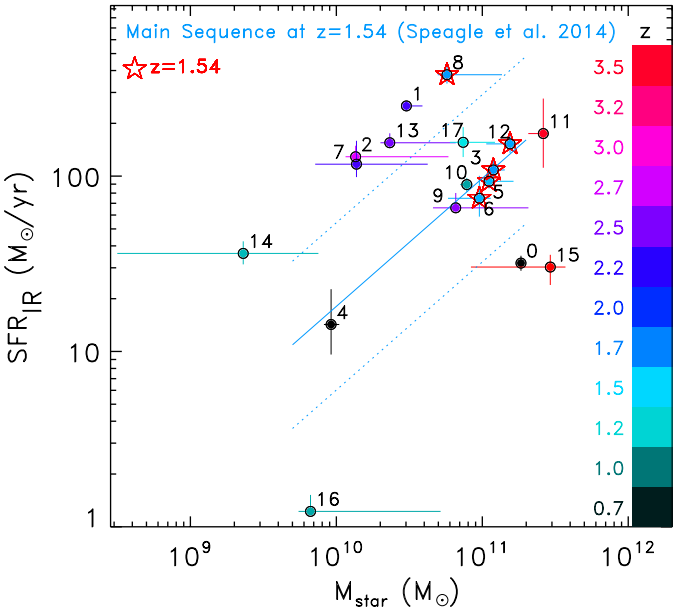

Fig. 10. SFR as a function of stellar mass for our 18 ALMA galaxies (full circles). The colours of the symbols represent photometric redshifts, as indicated by the vertical bar on the right-hand side. Filled circles decorated with stars indicate galaxies assumed to be at $z \simeq 1.54$. The blue line represents an MS relationship found for sources with an average redshift of $z = 1.5$ (Speagle et al. 2014), and the dashed lines indicate factors of 3 in SFR above and below the MS.

6.2. IRAM-30m/EMIR CO redshift

Observations of G073.4−57.5 were carried out using the heterodyne receiver EMIR (Carter et al. 2012) on the IRAM 30-m antenna between 13 September 2016 and 16 September 2016 (PID: 077-16, P.I: C. Martinache). We used the 3-mm band (E090) to search for CO transitions. The frequencies covered were 74–82 GHz; and 90–98 GHz. For the backends, we simultaneously used the wide-band line multiple auto-correlator (WILMA, 2-MHz spectral resolution) and the fast Fourier Transform Spectrometer (FTS200, 200-kHz resolution). Given that the observed object, SPIRE source 3 (ALMA field 2, see Table 2), is a point source, observations were performed in wobbler-switching mode with a throw of 30″. The beam size (HPBW) of IRAM 30-m/EMIR is 27″ at 91 GHz, comparable to the *Herschel*-SPIRE beam at 350 μm (25.15″). The total integration time is 300 min. For calibration, pointing, and focusing we used Jupiter, Mars, and bright quasars. Data reduction was performed with the help of the `CLASS` package, part of `GILDAS`. Baseline-removed spectra were co-added using the inverses of the squares of the individual noise levels as weights. We then fit the co-added spectra with a Gaussian profile and derived the line position, the peak flux and the line width (FHWM). The results are presented in Table 6.

In Fig. 11, middle panel, we show the EMIR spectrum together with the best-fit Gaussian curves for the EMIR data and the combined EMIR and ALMA data. We note a significant ($4.7\,\sigma$) detection very close (191 km s^{-1} separation) to the expected frequency of 90.64 GHz. In the joint fit the significance drops to $3.3\,\sigma$. We attribute the slight tension to either the low signal-to-noise in the EMIR data or to a physical difference between the gas components responsible for the excitations of the CO(5–4) and CO(2–1) line transitions, but take the EMIR spectrum as a strong indication for a CO(5–4) line in ALMA and a

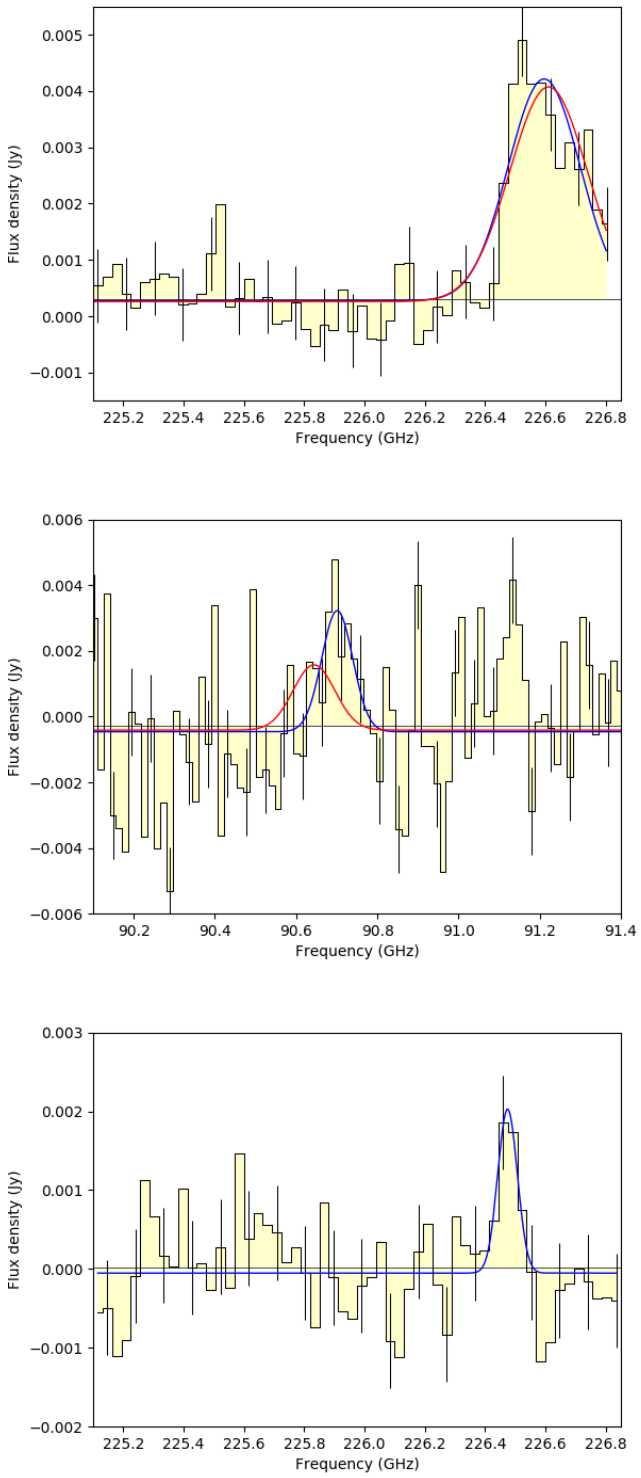

Fig. 11. Spectra of the two ALMA galaxies ID 3 (top and middle) and ID 8 (bottom), showing the serendipitous line detections, consistent with a CO(5–4) transition at $z = 1.54$. The blue Gaussian profiles show the best fits to each individual line. The red Gaussian profiles for ID 3 show the best combined fit to the CO(5–4) line in the ALMA spectrum (top) and the CO(2–1) line in the IRAM/EMIR spectrum (middle). The slight offset between the fitted line centres of 190 km s^{-1} seen in the EMIR data could be due to the low S/N or a physical difference between the transitions. Representative error bars per bin are shown for every third bin.

redshift of $z = 1.5434 \pm 0.0001$ from the joint fit (see Table 6); this is dominated by the high signal-to-noise ratio in the ALMA data (see the fitted Gaussian curves in Fig. 11, top panel). We assume, of course, that the EMIR line comes from ALMA ID 3 and not from another galaxy within the larger beam, and also not from another molecular species, since either of these options would be a rather unlikely coincidence.

6.3. CO line properties

Under the assumption that the detected line in ALMA is indeed CO(5–4), the CO luminosity can be calculated as (Solomon et al. 1997)

$$L'_{\rm CO} = \frac{c^2}{2k}\, S_{\rm CO}\, \Delta V\, \nu_{\rm sky}^{-2}\, D_{\rm L}^2\, (1+z)^{-3}. \quad (4)$$

Using the 400 km s^{-1} width estimate of the joint fit, we find that $L'_{\rm CO} = (1.5 \pm 0.1) \times 10^{10}$ K km s^{-1} pc^2. The CO(2–1) luminosity for the EMIR line is $L'_{\rm CO} = (3.2 \pm 1.0) \times 10^{10}$ K km s^{-1} pc^2, giving a ratio 2.1 relative to the CO(5–4) transition luminosity.

We also find tentative evidence for a faint line (S/N $\simeq$ 4.2 over four channels with two-channel Hanning smoothing) in ALMA galaxy ID 8 (the brightest in ALMA field 4), which has very similar NIR properties to those of ALMA galaxy ID 3 (see Fig. 4). At the peak intensity (226.47 GHz) of the Gaussian fit (see Table 6) the redshift is $z = 1.54491 \pm 0.00004$ for the same CO(5–4) transition. The integrated line flux density is (0.274 ± 0.062) Jy km s^{-1} at the (unresolved) peak, with line width (101 ± 31) km s^{-1}, and $L'_{\rm CO} = (1.5 \pm 0.3) \times 10^9$ K km s^{-1} pc^2. The dynamical mass estimate is $M_{\rm dyn} = 7.0 \times 10^9$ M$_\odot$, compared to a stellar mass of $M_* = 5.8 \times 10^{10}$ M$_\odot$ (from Table 5). The near coincidence of the frequency with that of ID 3 argues for the reality of this weaker line.

For these two galaxies, with the simple assumptions that $L'_{\rm CO(1-0)} = L'_{\rm CO(5-4)}$ and $\alpha_{\rm CO} = 0.8\,{\rm M}_\odot$ / K km s^{-1} pc^2 (Solomon et al. 1997), we could derive gas masses of 1.2×10^{10} M$_\odot$ (ID 3) and 1.1×10^9 M$_\odot$ (ID 8), which can be compared to $M_{\rm ISM}$ calculated from Eq. (2), i.e., 1.9×10^{11} M$_\odot$ (ID 3) and 1.2×10^{11} M$_\odot$ (ID 8). We note that the respective properties derived from $M_{\rm ISM}$ appear quite realistic: depletion times, $\tau_{\rm depl} = M_{\rm g}/{\rm SFR}$, are 1760 Myr and 390 Myr, and gas fractions, $f_{\rm g} = M_{\rm g}/(M_{\rm g} + M_\star)$, are 0.61 and 0.67. Thus, we argue that for the molecular mass a line ratio CO(5–4)/CO(1–0) of 2–3, as indicated also by the EMIR data, and an $\alpha_{\rm CO}$ of $\simeq$ 4 (for example, 4.3, as for spiral galaxies, see Bolatto et al. 2013), would be more plausible, and could bring the gas mass estimates into agreement.

In any case, there are large uncertainties involved with the conversion factors (see e.g., Daddi et al. 2015, for CO excitations) up to a factor of 5. Still, while source ID 3 is consistent with the $L_{\rm FIR}$–$L'_{\rm CO}$ relations derived by Greve et al. (2014) and Liu et al. (2015), for galaxy ID 8 the line flux is about an order of magnitude lower than expected.

Similarly, we can estimate how these galaxies compare with the Schmidt-Kennicutt relation (Kennicutt 1998),

$$\log \Sigma_{\rm SFR}/[{\rm M}_\odot\,{\rm yr}^{-1}\,{\rm kpc}^{-2}] = 1.42 \times \log \Sigma_{\rm gas}/[{\rm M}_\odot\,{\rm kpc}^{-2}] - 3.83, \quad (5)$$

as given by Daddi et al. (2010) in their figure 2, with a normalization that is 0.9 higher for starburst galaxies.

The SFR surface density, $\Sigma_{\rm SFR}$, is estimated to be $10^{0.78}$ M$_\odot$ yr^{-1} kpc^{-2} for ID 3, and $10^{1.54}$ M$_\odot$ yr^{-1} kpc^{-2} for ID 8 (accounting for a factor of 1.7 between the Chabrier and Salpeter

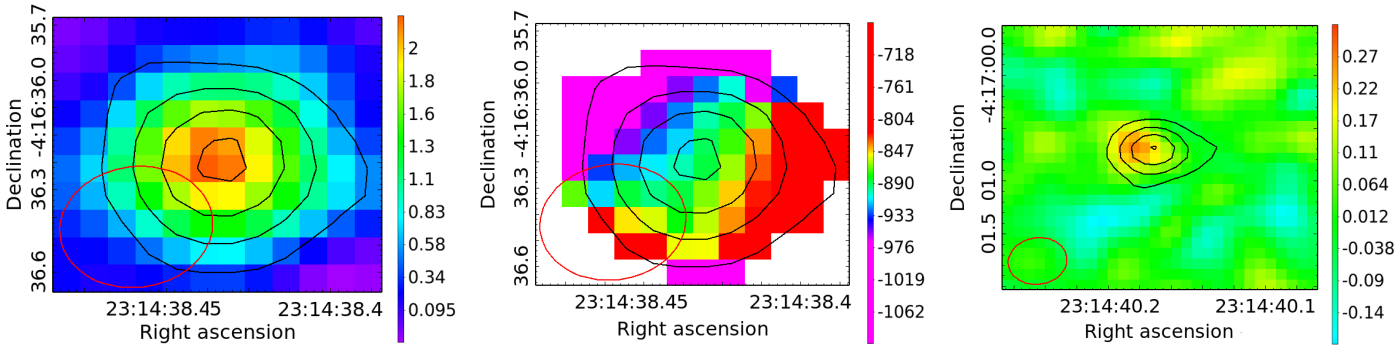

Fig. 12. Images on the left (ID 3) and on the right (ID 8) are of the integrated line emission in Jy km s^{-1} beam^{-1} (where the continuum has been subtracted). In both cases line and continuum emission (i.e., the black contours from $3\,\sigma = 0.18$ mJy in $3\,\sigma$ steps) coincide. In the middle, for the stronger line (ID 3) only, the first moment image in km s^{-1} is shown, also with continuum contours for reference. The FWHM of the synthesized beam is shown with red ellipses.

Table 6. Spectral fitting results for ALMA galaxies 3 and 8

ALMA ID	Data	$S_{\rm peak}$ [mJy]	Line width FWHM [km s^{-1}]	Redshift	Offset [mJy]
3	ALMA	3.9 ± 0.3	371 ± 38	1.54355 ± 0.00007	0.27 ± 0.10
3	EMIR	3.7 ± 0.8	296 ± 74	1.54178 ± 0.00010	−0.46 ± 0.12
3	ALMA joint	3.8 ± 0.3	401 ± 42	1.54338 ± 0.00013	−0.08 ± 0.08
3	EMIR joint	2.0 ± 0.6	401 ± 42	1.54338 ± 0.00013	−0.34 ± 0.08
8	ALMA	2.0 ± 0.5	101 ± 31	1.54491 ± 0.00004	−0.05 ± 0.08

IMFs). The H_2 surface density, $\Sigma_{\rm gas}$, can then be estimated using (again simplistically) a CO conversion of $\alpha_{\rm CO} = 0.8\,{\rm M}_\odot$ / K km s^{-1} pc^2 and a line ratio of $r_{54/10} = 1$; we find values of $10^{2.50}$ M$_\odot$ pc^{-2} for ID 3 and $10^{1.70}$ M$_\odot$ pc^{-2} for ID 8. ID 3 is consistent with the relation for high-z starburst galaxies, whereas ID 8 is two orders of magnitude above the expectation, rather extreme even with the considerable scatter in this relation. We note, that for ID 8 the continuum is seen to be extended (cf. Table 1) and the line emission in Fig. 12 is not, whereas for ID 3 the match of the emission processes is excellent. Comparing their masses to those derived from the CO luminosity, in both cases it appears that the gas masses could be substantially underestimated. However, we should remember that these scaling relations and FIR-derived parameters are highly uncertain.

We could not find any evidence for similar line emission from the other sources that have photo-z estimates at $z \simeq 1.5$.

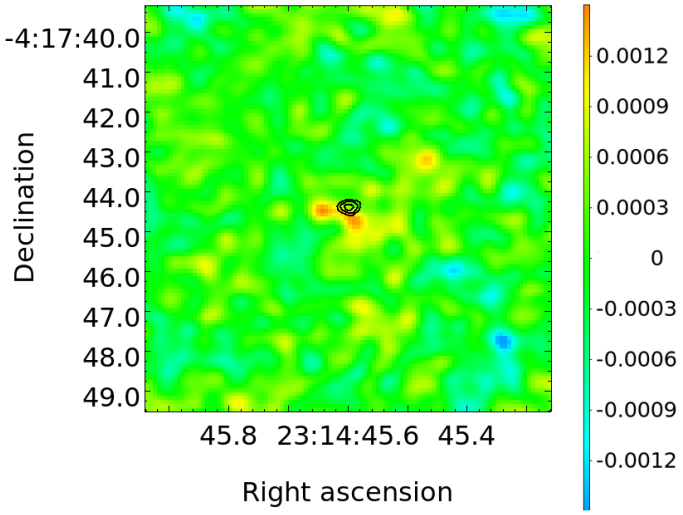

Fig. 13. Image at 226.49 GHz for ALMA ID 1 (colour scale in Jy beam^{-1}), showing two peaks of 3.5–4 σ each in the vicinity ($< 1''$) of the continuum emission (shown as the black contours, starting from 0.18 mJy in 0.06 mJy steps, i.e., $3\,\sigma$, $4\,\sigma$, and $5\,\sigma$).

7. Discussion

We have found that the ALMA detected galaxies comprising this *Planck* peak are primarily main-sequence galaxies that break up into redshift groups, with the galaxies associated with individual *Herschel* flux regions not necessarily falling into the same redshift ranges.

Consistently with the redshift for the serendipitous line detections, we find that the photo-z results for the majority of ALMA-detected galaxies cluster around $z \simeq 1.5$ (see Fig. 7). A significant fraction of galaxies appear to be closer, $z \lesssim 1$, but it is unclear whether they reside in a single structure. Given the large number of galaxies at $z \simeq 1.5$ and the matching spectroscopic redshifts of some, a physical association there seems rather likely. However, a few galaxies could also lie at between redshifts 2 and 3.

ALMA fields 5 and 8, where only a single ALMA galaxy was observed, are simple to interpret and in both cases have low ($z \simeq 1$) redshift. The central galaxy of field 1, ID 0, is likely at low redshift, $z \lesssim 1$, while its neighbour, ID 1, has a high photometric redshift, $z \simeq 2$–3. ID 3, the central galaxy for field 2, has a photometric redshift consistent with the spectroscopic redshift $z = 1.54$, while its nearest neighbours, IDs 2 and 4, are high and low redshift candidates, respectively. In field 3 all galaxies (IDs 5, 6, and 7) could be $z \simeq 1.5$ group members (although the latter two have a broad redshift range, particularly ID 7 could be at $z \simeq 2$–3). The galaxies, IDs 8 and 9 in field 4 are very close to each other (within one SPIRE pixel), making a deblending of the *Herschel* flux almost impossible and interpretation difficult. ID 9 fits with the $z \simeq 2$–3 group, and as discussed in the previous section, the photometric redshift assigned to ID 8 favours a redshift

of $z \simeq 1.5$ (when using the deblended *Herschel* fluxes), in agreement with the line detection at redshift $z = 1.54$. Despite their relative proximity, the two galaxies could be at different redshift. In field 6, ID 12 is the central source and at $z \simeq 1.5$, accompanied by ID 11, which has a redshift estimate with a very large uncertainty range, which overlaps with the redshift of ID 12 and could therefore be associated. Lastly, in ALMA field 7, where the *Herschel* source is weak, ALMA galaxies IDs 13 and 14 seem to be the main flux contributors. The uncertainties are large and the ranges overlapping, but 14 appears to to be at lower redshift than 13. The nature of ALMA IDs 15 and 16 are less clear; 16 could be at $z \simeq 1$, while 15 seems to be at higher redshift. However, due to the large number of sources within a very faint *Herschel* flux region, the deblending results are not very reliable here.

We note that of the six ALMA galaxies identified as possible starbursts (1, 2, 7, 8, 13, and 14), the two most significant (1 and 8) also show line emission (or indications of line emission), and might be associated with a $z \simeq 1.5$ structure. ALMA galaxy ID 3, which has by far the strongest detected line emission, has a star-formation rate similar to average MS galaxies. With velocity separations of less than $100\,\mathrm{km\,s^{-1}}$, ALMA galaxies IDs 1, 3, and 8 are thus likely to be part of the same physical structure. It appears that a good fraction of the high redshift structure members are undergoing vigorous star-formation and emitting strong CO lines, which means that the other members could also be detectable spectroscopically (unless in some galaxies star formation has been quenched and the gas depleted at $z \simeq 1.5$). On the other hand, it is possible that we did not detect lines from any other galaxies because they are centred outside of our observational spectral window. Indeed, the line of ALMA ID 3 clearly extends beyond the high frequency end of the spectral window, and the low frequency end is only $400\,\mathrm{km\,s^{-1}}$ away, corresponding to a redshift difference of only about 0.0013.

The tentative picture that emerges puts ALMA fields 1, 5, and 8 at $z \simeq 1$ and ALMA fields 2, 3, 4, 6, and 7 at $z \simeq 1.5$. But reality may not be quite so simple, as evidenced by the various "interlopers" found in several of the fields, which seem to indicate that some fields cannot really be categorized as belonging to one group or the other, but contain mixtures of high and low redshift galaxies. Broadly speaking, however, the nature of G073.4−57.5 seems to be at least two line-of-sight groups or clusters of galaxies at $z \simeq 1$ and $z \simeq 1.5$, and probably a few other galaxies at different redshifts. This conclusion also seems reasonable, since G073.4−57.5 appears similar to *Planck* peak G95.5−61.6 (Flores-Cacho et al. 2016) in the sense that it is a superposition of independent structures on the sky (in the case of G95.5−61.6 with two groups at $z = 1.7$ and $z = 2.0$).

Going back to the *Spitzer* and CFHT colour-magnitude and colour-colour diagrams (Figs. 4, 5, and 6) we can note that in particular for ALMA IDs 3, 5, and 8 their locations appear to be in good agreement with the photo-z results and our interpretation, while the other $z \simeq 1.5$ candidates IDs 6, 7, and 12, show reasonable consistency, in those diagrams where they were included (ALMA ID 14 had to be excluded from the colour analysis.

It is a valid question whether gravitational galaxy-galaxy lensing can play a role in enhancing the counts in a scenario where extended structures at lower and higher redshift overlap along the line of sight, giving apparent densities above typical "proto-cluster" measurements. In the current data most ALMA sources are well matched with *Spitzer* and NIR data and contain no indication of lensing signatures, while only a few sources show offsets, as seen in Fig. 3, between the mm and NIR emission (e.g., ALMA IDs 1, 4, 15), and possibly the gas (e.g., ALMA ID 1 in Fig. 13). In terms of statistical arguments, in general the probability for strong galaxy-galaxy lensing is small; for example, van der Wel et al. 2013 estimate one source per $200\,\mathrm{arcmin^2}$ for average counts of strongly lensed sources. However, lensing cannot be completely ruled out, and in particular smaller flux boosts by factors less than 2 could be common, since in our case the counts are enhanced (possibly by a factor of 10 for both the source and the lensed population), the redshift separation seems favourable, and of course the region was selected for high submm surface brightness in the first place.

8. Conclusions

Using ALMA, in only 24 minutes of on-source time we found 18 individual mm galaxies, showing that follow-up of the *Planck* high-z sample through targeted pointings of *Herschel*-SPIRE sources is an efficient use of this telescope. For the first time we are directly resolving the *Planck* peaks and *Herschel*-SPIRE overdensities into individual galaxies at mm wavelengths. The ALMA detections are well matched with *Spitzer*-IRAC sources in all but one cases and mostly show excellent positional agreement (typically $< 0.4''$); three sources that are offset by up to $1''$ are extended in *Spitzer*, and may either be blended or have intrinsically more complex structure.

The density of the mm galaxies within the ALMA pointings is 8–30 times higher than the average counts, and we estimate a total SFR $2100\,\mathrm{M_\odot\,yr^{-1}}$ (of which $900\,\mathrm{M_\odot\,yr^{-1}}$ can be attributed to sources with photo-zs consistent with $z \simeq 1.5$). Furthermore, the SCUBA-2 data indicate that we have not recovered all of the mm galaxies in this field, possibly not even the brightest, which will require a wider mosaic. Nevertheless, we can conclude that the *Planck* peak G073.4−57.5 consists of a large number of moderately bright mm galaxies, rather than a few extremely bright galaxies. Typical "proto-clusters" (such as the COSMOS $z = 2.47$ structure or the SSA22 $z = 3.09$ structure) contain fewer galaxies than we have detected, perhaps because G073.4−57.5 is a line-of-sight superposition of two massive structures. The cluster XCS J2215.9−1738 at $z = 1.46$ also shows a high density of ALMA galaxies, but those are fainter.

NIR colour diagrams of the ALMA detected galaxies reveal a "red sequence," a characteristic feature of $z > 1.3$ structures that are the progenitors of later massive galaxy clusters. FIR+NIR photo-z analysis indicates a concentration at $z \simeq 1.5$, while a second structure at lower redshift ($z \simeq 1$) could be present as well, in-line with the interpretation of two line-of-sight structures. In addition to photometric redshifts, we present SFRs, IR luminosities, stellar masses, dust temperatures, and dust masses for the galaxies. Three galaxies at $z \simeq 1$–2 can clearly be identified as starbursts (i.e., lying a factor 3 or more above the MS), while most of the galaxies are within the normal range of star-formation rates for their stellar masses.

Serendipitous line detections of two (possibly three) galaxies at a common frequency ($\Delta V < 100\,\mathrm{km\,s^{-1}}$) are interpreted as the CO(5–4) transition and can be used to fix the redshift of the main structure to $z = 1.54338 \pm 0.00013$, in agreement with the photo-z estimates. However, this needs to be confirmed with additional spectroscopy.

There are several important aspects to be followed up. Firstly, optical/NIR or mm spectroscopy (see e.g., Casey et al. 2017) will allow us to confirm the photo-z estimates and the association of the individual galaxies with structures in redshift space. Secondly, it will be helpful to associate all SCUBA-2 sources with their counterparts in ALMA data in order to study

those brightest submm peaks in more detail. Thirdly, it is important to address the positional offsets between the NIR and FIR images with future high-resolution data, in particular by searching for elongations or multiple images, which would be evidence of strong lensing. Lastly, further imaging and spectroscopy of this *Planck* peak will enable us to characterize its physical properties in terms of angular and redshift space morphology and to build a census of its stellar and star-forming properties. Such a detailed study is the only way to determine the nature of these red peaks in the CIB that have been picked out by *Planck*, which is the most decisive step in determining what exactly they are teaching us about structure formation.

Acknowledgements. This work is mainly based on the following ALMA data: ADS/JAO.ALMA# 2013.1.01173.S. ALMA is a partnership of ESO (representing its member states), NSF (USA) and NINS (Japan), together with NRC (Canada), NSC, and ASIAA (Taiwan), and KASI (Republic of Korea), in cooperation with the Republic of Chile. The Joint ALMA Observatory is operated by ESO, AUI/NRAO and NAOJ. The development of *Planck* has been supported by: ESA; CNES and CNRS/INSU-IN2P3-INP (France); ASI, CNR, and INAF (Italy); NASA and DoE (USA); STFC and UKSA (UK); CSIC, MICINN, JA, and RES (Spain); Tekes, AoF, and CSC (Finland); DLR and MPG (Germany); CSA (Canada); DTU Space (Denmark); SER/SSO (Switzerland);RCN (Norway); SFI (Ireland); FCT/MCTES (Portugal); and PRACE (EU). *Herschel* is an ESA space observatory with science instruments provided by European-led Principal Investigator consortia and with important participation from NASA. This work is based in part on observations made with the Spitzer Space Telescope, which is operated by the Jet Propulsion Laboratory, California Institute of Technology under a contract with NASA. MP acknowledges financial support from Labex OCEVU. This work has been carried out thanks to the support of the OCEVU Labex (ANR-11-LABX-0060) and the A*MIDEX project (ANR-11-IDEX-0001-02) funded by the "Investissements d'Avenir" French government programme managed by the ANR. This research has made use of the NASA/ IPAC Infrared Science Archive, which is operated by the Jet Propulsion Laboratory, California Institute of Technology, under contract with the National Aeronautics and Space Administration. This publication makes use of data products from the Wide-field Infrared Survey Explorer, which is a joint project of the University of California, Los Angeles, and the Jet Propulsion Laboratory/California Institute of Technology, and NEOWISE, which is a project of the Jet Propulsion Laboratory/California Institute of Technology; WISE and NEOWISE are funded by the National Aeronautics and Space Administration. This work was supported by the Natural Sciences and Research Council of Canada. The James Clerk Maxwell Telescope has historically been operated by the Joint Astronomy Centre on behalf of the Science and Technology Facilities Council of the United Kingdom, the National Research Council of Canada and the Netherlands Organisation for Scientific Research. Additional funds for the construction of SCUBA-2 were provided by the Canada Foundation for Innovation. The Pan-STARRS1 Surveys (PS1) and the PS1 public science archive have been made possible through contributions by the Institute for Astronomy, the University of Hawaii, the Pan-STARRS Project Office, the Max-Planck Society and its participating institutes, the Max Planck Institute for Astronomy, Heidelberg and the Max Planck Institute for Extraterrestrial Physics, Garching, The Johns Hopkins University, Durham University, the University of Edinburgh, the Queen's University Belfast, the Harvard-Smithsonian Center for Astrophysics, the Las Cumbres Observatory Global Telescope Network Incorporated, the National Central University of Taiwan, the Space Telescope Science Institute, the National Aeronautics and Space Administration under Grant No. NNX08AR22G issued through the Planetary Science Division of the NASA Science Mission Directorate, the National Science Foundation Grant No. AST-1238877, the University of Maryland, Eotvos Lorand University (ELTE), the Los Alamos National Laboratory, and the Gordon and Betty Moore Foundation.

References

Becker, R. H., White, R. L., & Helfand, D. J. 1995, ApJ, 450, 559
Berta, S., Lutz, D., Santini, P., et al. 2013, A&A, 551, A100
Bertin, E. & Arnouts, S. 1996, A&AS, 117, 393
Blain, A. W., Chapman, S. C., Smail, I., & Ivison, R. 2004, ApJ, 611, 725
Blain, A. W. & Longair, M. S. 1993, MNRAS, 264, 509
Bolatto, A. D., Wolfire, M., & Leroy, A. K. 2013, ARA&A, 51, 207
Bolzonella, M., Miralles, J.-M., & Pelló, R. 2000, A&A, 363, 476
Brammer, G. B., van Dokkum, P. G., & Coppi, P. 2008, ApJ, 686, 1503
Bruzual, G. & Charlot, S. 2003, MNRAS, 344, 1000
Cañameras, R., Nesvadba, N., Kneissl, R., et al. 2017a, ArXiv e-prints
Cañameras, R., Nesvadba, N. P. H., Guery, D., et al. 2015, A&A, 581, A105
Cañameras, R., Nesvadba, N. P. H., Kneissl, R., et al. 2017b, A&A, 600, L3
Capak, P. L., Riechers, D., Scoville, N. Z., et al. 2011, Nature, 470, 233
Carilli, C. L. & Walter, F. 2013, ARA&A, 51, 105
Carniani, S., Maiolino, R., De Zotti, G., et al. 2015, A&A, 584, A78
Carter, M., Lazareff, B., Maier, D., et al. 2012, A&A, 538, A89
Casey, C. M. 2016, ApJ, 824, 36
Casey, C. M., Chen, C.-C., Cowie, L. L., et al. 2013, MNRAS, 436, 1919
Casey, C. M., Cooray, A., Capak, P., et al. 2015, ApJ, 808, L33
Casey, C. M., Cooray, A., Killi, M., et al. 2017, ArXiv e-prints
Chabrier, G. 2003, PASP, 115, 763
Chambers, K. C., Magnier, E. A., Metcalfe, N., et al. 2016, ArXiv e-prints
Clements, D. L., Dunne, L., & Eales, S. 2010, MNRAS, 403, 274
da Cunha, E., Walter, F., Smail, I. R., et al. 2015, ApJ, 806, 110
Daddi, E., Dannerbauer, H., Liu, D., et al. 2015, A&A, 577, A46
Daddi, E., Elbaz, D., Walter, F., et al. 2010, ApJ, 714, L118
Dale, D. A., Aniano, G., Engelbracht, C. W., et al. 2012, ApJ, 745, 95
Danielson, A. L. R., Swinbank, A. M., Smail, I., et al. 2017, ApJ, 840, 78
Davidzon, I., Ilbert, O., Laigle, C., et al. 2017, A&A, 605, A70
Draine, B. T. 2011, Physics of the Interstellar and Intergalactic Medium (Princeton: Princeton University Press)
Dunlop, J. S., McLure, R. J., Biggs, A. D., et al. 2017, MNRAS, 466, 861
Flores-Cacho, I., Pierini, D., Soucail, G., et al. 2016, A&A, 585, A54
Franx, M., Labbé, I., Rudnick, G., et al. 2003, ApJ, 587, L79
Fujimoto, S., Ouchi, M., Ono, Y., et al. 2016, ApJS, 222, 1
González-López, J., Bauer, F. E., Romero-Cañizales, C., et al. 2016, A&A, 597, A41
Greve, T. R., Leonidaki, I., Xilouris, E. M., et al. 2014, ApJ, 794, 142
Guiderdoni, B., Bouchet, F. R., Puget, J.-L., Lagache, G., & Hivon, E. 1997, Nature, 390, 257
Hatch, N. A., Muldrew, S. I., Cooke, E. A., et al. 2016, MNRAS, 459, 387
Hatsukade, B., Kohno, K., Umehata, H., et al. 2016, PASJ, 68, 36
Hatsukade, B., Ohta, K., Seko, A., Yabe, K., & Akiyama, M. 2013, ApJ, 769, L27
Hayashi, M., Kodama, T., Kohno, K., et al. 2017, ApJ, 841, L21
Hayashi, M., Kodama, T., Tadaki, K.-i., Koyama, Y., & Tanaka, I. 2012, ApJ, 757, 15
Kennicutt, Jr., R. C. 1998, ARA&A, 36, 189
Kodama, T., Arimoto, N., Barger, A. J., & Arag'on-Salamanca, A. 1998, A&A, 334, 99
Lacy, M., Wilson, G., Masci, F., et al. 2005, ApJS, 161, 41
Lilly, S. J., Eales, S. A., Gear, W. K. P., et al. 1999, ApJ, 518, 641
Liu, D., Gao, Y., Isaak, K., et al. 2015, ApJ, 810, L14
MacKenzie, T. P., Scott, D., Bianconi, M., et al. 2017, MNRAS, 468, 4006
Mainzer, A., Bauer, J., Grav, T., et al. 2011, ApJ, 731, 53
Martinache, C. 2016, PhD Thesis, IAS, Univ. Paris-Sud, Orsay
McMullin, J. P., Waters, B., Schiebel, D., Young, W., & Golap, K. 2007, in Astronomical Society of the Pacific Conference Series, Vol. 376, Astronomical Data Analysis Software and Systems XVI, ed. R. A. Shaw, F. Hill, & D. J. Bell, 127
Muzzin, A., Marchesini, D., Stefanon, M., et al. 2013, ApJ, 777, 18
Narayanan, D., Turk, M., Feldmann, R., et al. 2015, Nature, 525, 496
Nesvadba, N., Kneissl, R., Cañameras, R., et al. 2016, A&A, 593, L2
Ono, Y., Ouchi, M., Kurono, Y., & Momose, R. 2014, ApJ, 795, 5
Oteo, I., Zwaan, M. A., Ivison, R. J., Smail, I., & Biggs, A. D. 2016, ApJ, 822, 36
Overzier, R. A. 2016, A&A Rev., 24, 14
Papovich, C. 2008, ApJ, 676, 206
Pilbratt, G. L., Riedinger, J. R., Passvogel, T., et al. 2010, A&A, 518, L1
Planck Collaboration, Abergel, A., Ade, P. A. R., et al. 2011, A&A, 536, A21
Planck Collaboration, Ade, P. A. R., Aghanim, N., et al. 2014a, A&A, 571, A1
Planck Collaboration, Ade, P. A. R., Aghanim, N., et al. 2014b, A&A, 571, A18
Planck Collaboration, Ade, P. A. R., Aghanim, N., et al. 2016a, A&A, 594, A13
Planck Collaboration, Ade, P. A. R., Aghanim, N., et al. 2016b, A&A, 596, A100
Planck Collaboration, Aghanim, N., Altieri, B., et al. 2015, A&A, 582, A30
Polletta, M., Tajer, M., Maraschi, L., et al. 2007, ApJ, 663, 81
Rettura, A., Martinez-Manso, J., Stern, D., et al. 2014, ApJ, 797, 109
Scoville, N., Aussel, H., Sheth, K., et al. 2014, ApJ, 783, 84
Scoville, N., Sheth, K., Aussel, H., et al. 2016, ApJ, 820, 83
Solomon, P. M., Downes, D., Radford, S. J. E., & Barrett, J. W. 1997, ApJ, 478, 144
Speagle, J. S., Steinhardt, C. L., Capak, P. L., & Silverman, J. D. 2014, ApJS, 214, 15
Stach, S. M., Swinbank, A. M., Smail, I., Hilton, M., & Simpson, J. M. 2017, ArXiv e-prints
Swinbank, A. M., Lacey, C. G., Smail, I., et al. 2008, MNRAS, 391, 420
Swinbank, A. M., Simpson, J. M., Smail, I., et al. 2014, MNRAS, 438, 1267

Umehata, H., Tamura, Y., Kohno, K., et al. 2015, ApJ, 815, L8
Umehata, H., Tamura, Y., Kohno, K., et al. 2017, ApJ, 835, 98
van der Wel, A., van de Ven, G., Maseda, M., et al. 2013, ApJ, 777, L17
Vieira, J. D., Marrone, D. P., Chapman, S. C., et al. 2013, Nature, 495, 344
Wright, E. L., Eisenhardt, P. R. M., Mainzer, A. K., et al. 2010, AJ, 140, 1868

Appendix A: Photometric redshift fit results

Figure A1 shows our multi-wavelength flux density measurements as black circles and the best-fit templates obtained in the second round of `Hyper-z` fitting using template libraries from Polletta et al. (2007), Danielson et al. (2017), and da Cunha et al. (2015) as magenta curves. For comparison we also show the fits performed using `EAZY` (Brammer et al. 2008) as orange curves. Downward arrows correspond to $3\,\sigma$ upper limits and are shown in the cases where the flux density detection was below $2\,\sigma$. The green curve is the best-fit model obtained by fitting the WIRCam-IRAC SED with models by Bruzual & Charlot (2003). The purple curve represents the best-fit to the far-IR SED obtained using a single-temperature modified blackbody model. The dashed red and cyan curves represent, respectively, the highest and lowest temperature modified blackbody model consistent with the far-IR SED within $1\,\sigma$. For comparison, the blue curve is the best-fit model obtained by fixing the redshift to the precise value of $z = 1.54$, assumed from the lines found in ALMA IDs 3 and 8. The ALMA ID and photometric redshifts are annotated in the top left corners of each panel. The spectroscopic redshift is annotated in the top right corner of each panel, when available.

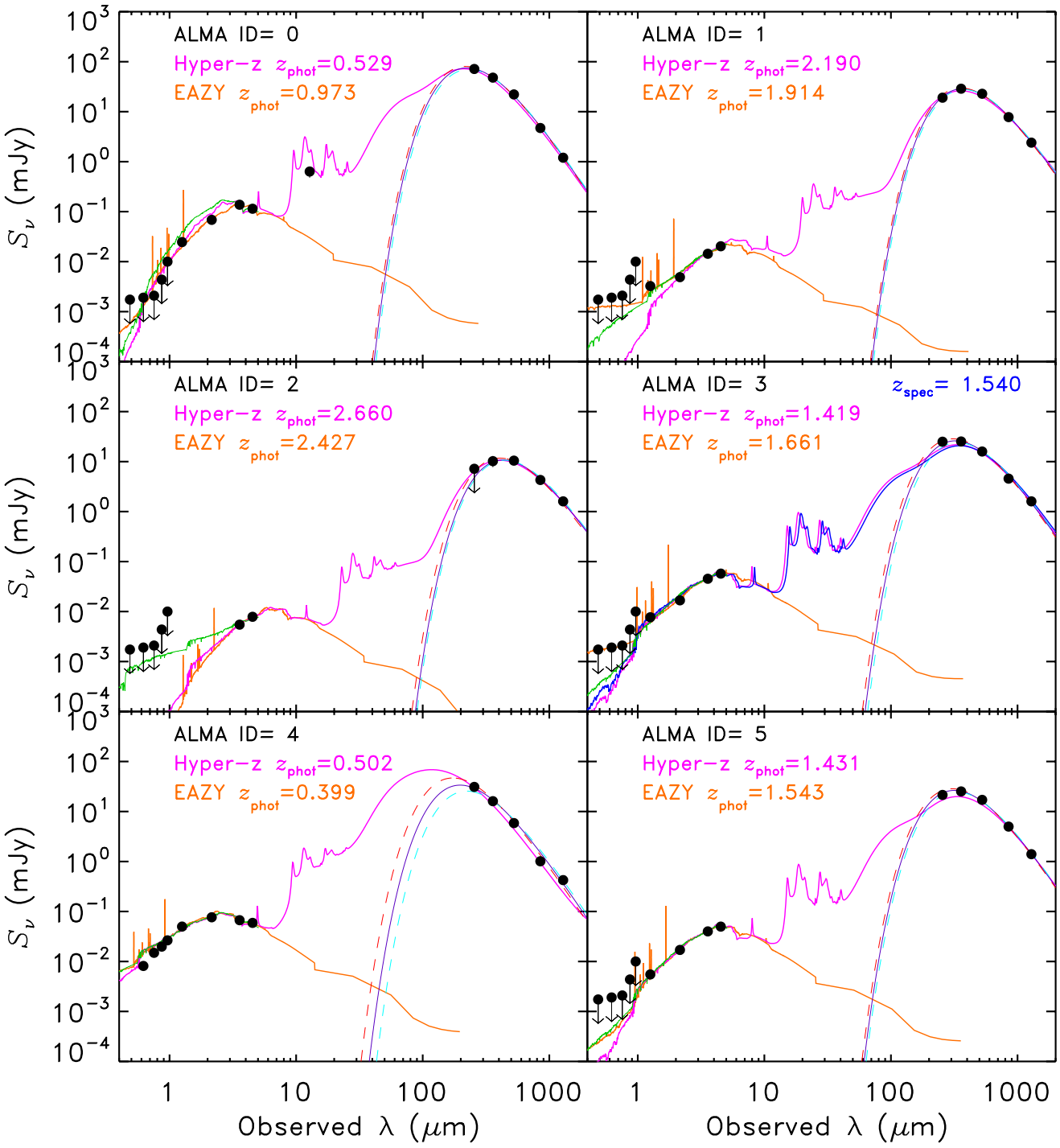
ALMA ID= 0
Hyper−z z_{phot}=0.529
EAZY z_{phot}=0.973
ALMA ID= 1
Hyper−z z_{phot}=2.190
EAZY z_{phot}=1.914
ALMA ID= 2
Hyper−z z_{phot}=2.660
EAZY z_{phot}=2.427
ALMA ID= 3
z_{spec}= 1.540
Hyper−z z_{phot}=1.419
EAZY z_{phot}=1.661
ALMA ID= 4
Hyper−z z_{phot}=0.502
EAZY z_{phot}=0.399
ALMA ID= 5
Hyper−z z_{phot}=1.431
EAZY z_{phot}=1.543
S_ν (mJy)
Observed λ (μm)
1
10
100
1000

Fig. A.1.

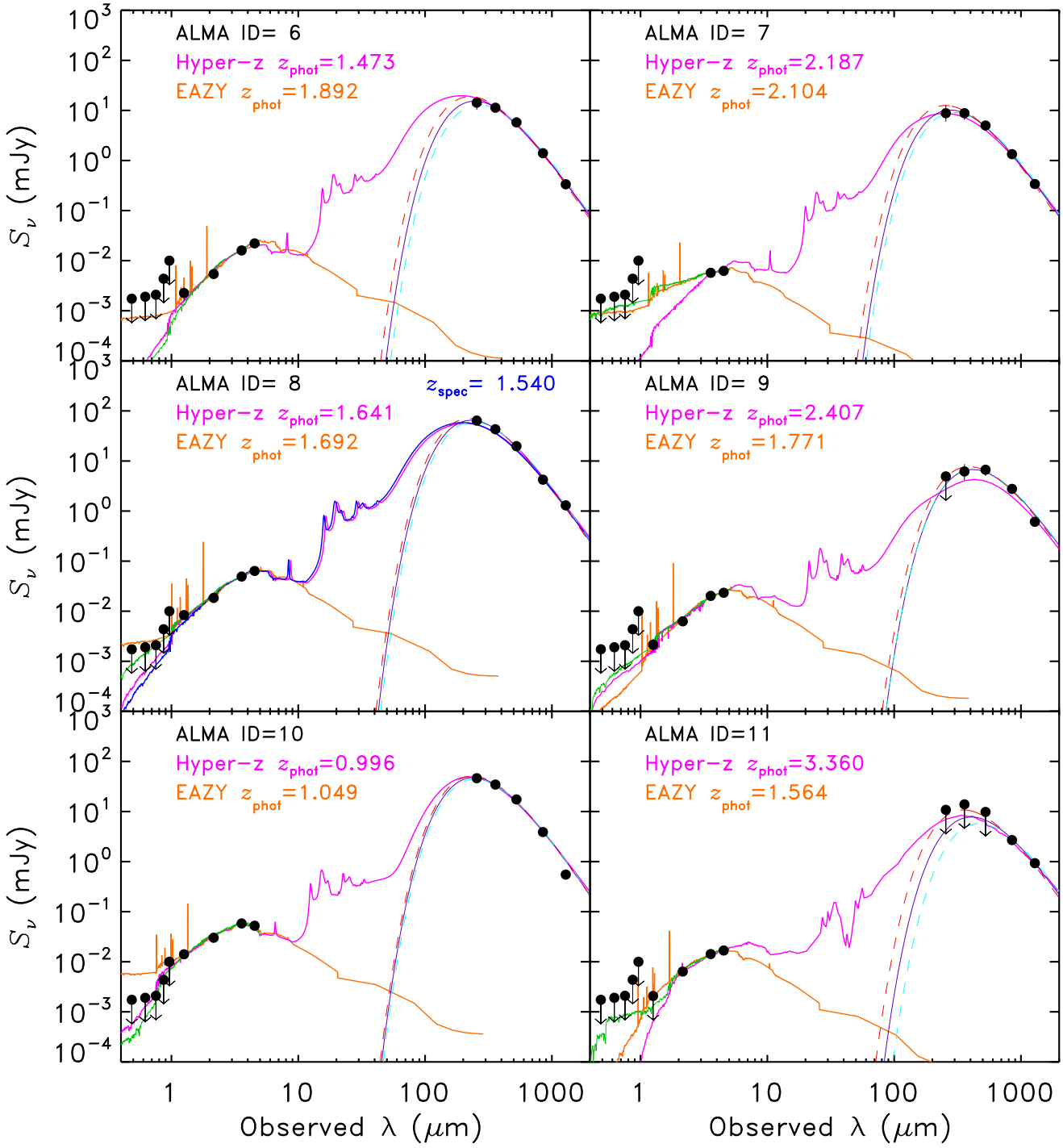

Fig. A.1. Continued.

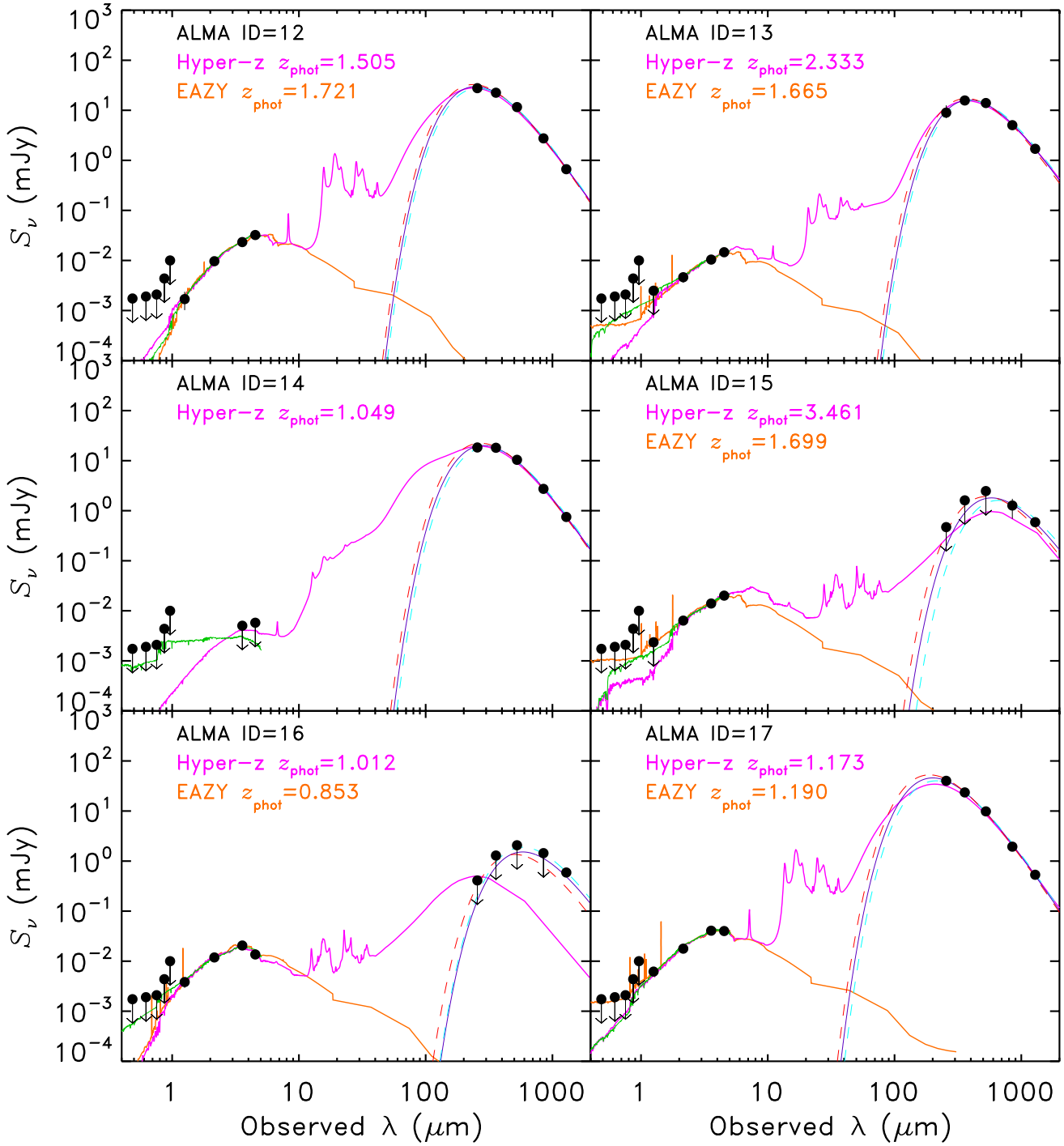

Fig. A.1. Continued.